

Central Lancashire Online Knowledge (CLoK)






Title	The interplay between accretion, galaxy downsizing and the formation of box/peanut bulges in TNG50
Type	Article
URL	https://clock.uclan.ac.uk/id/eprint/45829/
DOI	https://doi.org/10.1093/mnras/stad3271
Date	2023
Citation	Anderson, Stuart, Gough-Kelly, Steven, Debattista, Victor P, Du, Min, Erwin, Peter, Cuomo, Virginia, Caruana, Joseph, Hernquist, Lars and Vogelsberger, Mark (2023) The interplay between accretion, galaxy downsizing and the formation of box/peanut bulges in TNG50. Monthly Notices of the Royal Astronomical Society. ISSN 0035-8711
Creators	Anderson, Stuart, Gough-Kelly, Steven, Debattista, Victor P, Du, Min, Erwin, Peter, Cuomo, Virginia, Caruana, Joseph, Hernquist, Lars and Vogelsberger, Mark

It is advisable to refer to the publisher's version if you intend to cite from the work.
<https://doi.org/10.1093/mnras/stad3271>

For information about Research at UCLan please go to <http://www.uclan.ac.uk/research/>

All outputs in CLoK are protected by Intellectual Property Rights law, including Copyright law. Copyright, IPR and Moral Rights for the works on this site are retained by the individual authors and/or other copyright owners. Terms and conditions for use of this material are defined in the <http://clock.uclan.ac.uk/policies/>

The interplay between accretion, downsizing, and the formation of box/peanut bulges in TNG50

Stuart Robert Anderson ¹★, Steven Gough-Kelly ¹, Victor P. Debattista ^{1,2}, Min Du,³ Peter Erwin ^{4,5}, Virginia Cuomo,⁶ Joseph Caruana,^{2,7} Lars Hernquist⁸ and Mark Vogelsberger ⁹

¹Jeremiah Horrocks Institute, University of Central Lancashire, Preston PR1 2HE, UK

²Institute of Space Sciences & Astronomy, University of Malta, Msida MSD 2080, Malta

³Department of Astronomy, Xiamen University, Xiamen, Fujian 361005, China

⁴Max-Planck-Institut für extraterrestrische Physik, Giessenbachstrasse, D-85748 Garching, Germany

⁵Universitäts-Sternwarte München, Scheinerstrasse 1, D-81679 München, Germany

⁶Instituto de Astronomía y Ciencias Planetarias, Universidad de Atacama, Avenida Copayapu 485, 1350000 Copiapó, Chile

⁷Department of Physics, Faculty of Science, University of Malta, Msida MSD 2080, Malta

⁸Harvard-Smithsonian Center for Astrophysics, 60 Garden Street, Cambridge, MA 02138, USA

⁹Department of Physics and Kavli Institute for Astrophysics and Space Research, Massachusetts Institute of Technology, Cambridge, MA 02139, USA

Accepted 2023 October 19. Received 2023 October 19; in original form 2023 February 23

ABSTRACT

From the TNG50 cosmological simulation we build a sample of 191 well-resolved barred galaxies with stellar mass $\log(M_*/M_\odot) > 10$ at $z = 0$. We search for box/peanut bulges (BPs) in this sample, finding them in 55 per cent of cases. We compute f_{BP} , the BP probability for barred galaxies as a function of M_* , and find that this rises to a plateau, as found in observations of nearby galaxies. The transition mass where f_{BP} reaches half the plateau value is $\log(M_*/M_\odot) = 10.13 \pm 0.07$, consistent with the observational value within measurement errors. We show that this transition in f_{BP} can be attributed to the youth of the bars at low M_* , which is a consequence of downsizing. Young bars, being generally shorter and weaker, have not yet had time to form BPs. At high mass, while we find a plateau, the value is at ~ 60 per cent whereas observations saturate at 100 per cent. We attribute this difference to excessive heating in TNG50 due to merger activity and numerical resolution effects. BPs in TNG50 tend to occur in galaxies with more quiescent merger histories. As a result, the main driver of whether a bar hosts a BP in TNG50 is not the galaxy mass, but how long and strong the bar is. Separating the BP sample into those that have visibly buckled and those that have not, we find that fully half of BP galaxies show clear signs of buckling, despite the excessive heating and limited vertical resolution of TNG50.

Key words: galaxies: bulges – galaxies: evolution – galaxies: kinematics and dynamics – galaxies: structure.

1 INTRODUCTION

Box/peanut bulges (BPs) are the vertically extended inner portions of some galactic bars, with a characteristic ‘X’ shape when viewed side-on. Bars are present in most disc galaxies (Eskridge et al. 2000; Marinova & Jogee 2007; Menendez-Delmestre et al. 2007; Erwin 2018, 2019) and are key drivers of much of their secular evolution (Weinberg 1985; Debattista & Sellwood 1998; Athanassoula 2002, 2003; Athanassoula & Misiriotis 2002; Kormendy & Kennicutt 2004; Holley-Bockelmann, Weinberg & Katz 2005; Debattista et al. 2006; Ceverino & Klypin 2007; Dubinski, Berentzen & Shlosman 2009). The Milky Way (MW) also has a BP (McWilliam & Zoccali 2010; Nataf et al. 2010, and references therein). Therefore an understanding of galaxy evolution, including of the MW, requires a detailed understanding of the conditions under which BPs form.

Observationally, Erwin & Debattista (2017, hereafter ED17) studied 84 local barred galaxies from the Spitzer Survey of Stellar Structure in Galaxies (S⁴G; Sheth et al. 2010), finding the fraction of BPs amongst barred galaxies to be a strong function of stellar mass, and that above a stellar mass $\log(M_*/M_\odot) \simeq 10.4$ the majority of barred galaxies host BPs. This was updated with a larger data set of 132 galaxies (Erwin, Debattista & Anderson 2023, hereafter EDA23), yielding a turning point of $\log(M_*/M_\odot) \simeq 10.3$. Using kinematic signatures, Gadotti et al. (2020) found a fraction of 62 per cent BPs in a sample of 21 massive barred galaxies from the MUSE TIMER project. Marchuk et al. (2022) also found an upturn in BP fraction at $\log(M_*/M_\odot) \simeq 10.4$ in their sample of 483 edge-on galaxies from the Dark Energy Spectroscopic Instrument survey, albeit with a much lower fraction overall.

BPs have been studied in detail in simulations (e.g. Raha et al. 1991; Berentzen et al. 1998; Athanassoula & Misiriotis 2002; Bureau & Athanassoula 2005; Martinez-Valpuesta, Shlosman & Heller 2006; Saha & Gerhard 2013; Debattista et al. 2017; Fragkoudi et al. 2017; Saha, Graham & Rodríguez-Herranz 2018; Łokas 2019;

* E-mail: sra.ngc1300@gmail.com

Ciambur et al. 2021). They show that one formation mechanism for BPs is the buckling instability (Raha et al. 1991; Merritt & Sellwood 1994; Martinez-Valpuesta & Shlosman 2004; Smirnov & Sotnikova 2019), a sudden asymmetric bending of the bar in its inner regions. Observations have recognized a few ($\lesssim 10$) galaxies currently undergoing buckling (Erwin & Debattista 2016; Li, Ho & Barth 2017; Xiang et al. 2021). Strong buckling produces long-lasting asymmetries about the mid-plane, which may be recognized for a few Gyr in edge-on galaxies, but these have not yet been detected (Cuomo et al. 2022). An alternative BP formation mechanism, the trapping of stellar orbits into vertical resonances, is more gradual (Combes & Sanders 1981; Combes et al. 1990; Quillen 2002; Sellwood & Gerhard 2020). What fraction of the observed BPs is produced by the two mechanisms is as yet unknown.

Large-volume galaxy formation simulations are now reaching resolutions where they can begin to capture realistic secular evolution for large samples of galaxies (Vogelsberger et al. 2020). While many studies of BP bulges have been in isolated simulations, there have been relatively few using cosmological simulations. Buck et al. (2018) studied a Milky Way-like galaxy from the NIHAO high-resolution zoom-in simulations, focusing on the BP. Debattista et al. (2019) studied a strongly barred galaxy with an ‘X’ shape from the FIRE cosmological suite, and found that the density bimodality of the ‘X’-shape decreases in strength with stellar age. Gargiulo et al. (2019) examined the 30 zoom-in simulations in the Auriga suite (Grand et al. 2017, 2019) specifically designed to replicate Milky Way-like galaxies, finding at least three with BPs at $z = 0$. Blázquez-Calero et al. (2020) examined 21 barred galaxies in the Auriga simulation and found four galaxies with BPs (19 percent) and an additional two which were buckling at $z = 0$. Using the same simulations, Fragkoudi et al. (2020) found five galaxies with BPs, and four with weak BPs, for a total fraction of ~ 30 per cent of barred galaxies, considerably lower than in observations.

In this study, we use the TNG50 simulation (Pillepich et al. 2019; Nelson et al. 2019a, b) to study galaxies with BPs at $z = 0$. TNG50 is the highest resolution run of the IllustrisTNG project (Vogelsberger et al. 2014a, b; Marinacci et al. 2018; Naiman et al. 2018; Nelson et al. 2018; Springel et al. 2018) to date and offers an unrivalled opportunity to investigate BP galaxies with reasonably high resolution. This simulation enables us to study a significantly larger self-consistent sample of BP galaxies than has previously been possible. The aim of this study is to provide insight into the conditions which lead to the formation of BPs with a statistically significant sample. We examine the BP fraction amongst barred galaxies, and discern BPs formed by strong buckling, and those formed by weak buckling or resonant trapping. We compare our findings to observations of the local Universe, analysing and offering explanations for any differences.

This paper is structured as follows. In Section 2, we briefly introduce the TNG50 simulation. The methods used to detect and measure bars and BPs are variations of techniques used previously and are presented in Appendix A. In Section 3, we present the fraction of BPs as a function of stellar mass in TNG50. In Section 4, we model the BP fraction as a function of various galactic characteristics, and in Section 5 we analyse the differences in evolution between the galaxies with BPs at $z = 0$ and those without. In Section 6, we examine the impact of bar age on the frequency of BPs, and in Section 7, we analyse the role of gas. We discuss the implications of our findings in Section 8 and summarize in Section 9. The reader interested in measurement details may wish to read the appendix right after Section 2.

2 TNG50

IllustrisTNG¹ (Vogelsberger et al. 2014a, b; Marinacci et al. 2018; Naiman et al. 2018; Nelson et al. 2018; Springel et al. 2018) is a suite of advanced cosmological simulations within the Λ CDM framework that employs magneto-hydrodynamics as well as a dual-mode thermal and kinematic black hole feedback model, described in detail in Weinberger et al. (2017) and Pillepich et al. (2018). The free parameters of the model were chosen to reproduce observed integrated trends of galactic properties.

We use the highest resolution run of the IllustrisTNG suite, TNG50, which simulated 2×2160^3 dark-matter particles and gas cells within a volume of side length $35/h$ or ~ 50 cMpc. Alongside a baryonic mass resolution of $8.5 \times 10^4 M_\odot$ and gravitational softening length for stellar particles of $\epsilon = 288$ pc ($1 \geq z \geq 0$), $\epsilon \sim 500$ pc ($z > 1$), the simulation also achieves gas cell sizes as small as 70 pc in dense star-forming regions. This creates large statistical samples of galaxies at ‘zoom’-like resolution (Pillepich et al. 2019; Nelson et al. 2019b).

The IllustrisTNG Collaboration identified dark matter haloes within the simulation at each time-step using the friends-of-friends algorithm (Davis et al. 1985); subhaloes within each halo were identified using the SUBFIND algorithm (Springel et al. 2001; Dolag et al. 2009). Galaxies are defined as gravitationally bound stellar masses within a halo or subhalo. In conducting our analysis, we extract all the bound particles (gas, stellar, and dark matter particles) within a (sub)halo associated with a galaxy and place the origin at the centre of the potential. We then rotate each galaxy by aligning the angular momentum vector within $2R_{\text{eff}}$ of the stellar disc with the z -axis, resulting in the stellar disc being in the (x, y) -plane. We extract the main leaf progenitor branch (Rodríguez-Gómez et al. 2015) for each of our sample galaxies.

While TNG50 has a large number of galaxies modelled with state-of-the-art subgrid physics, none the less it has some systematic effects which limit the analysis we can employ. In particular, at $z = 0$, TNG50 has a stellar force softening length of 288 pc. This means that at small distances, the force resolution is comparable to the disc thickness, and bending waves (such as those involved in the buckling instability) are not well captured (Merritt & Sellwood 1994). Hence dynamical processes are not fully resolved for small bars, and we remove galaxies with small bars ($R_{\text{bar}} < 2.6$ kpc) from our analysis (see Appendix A1 for a detailed discussion).

We emphasize that we only seek galaxies with BPs at the *current epoch*, examining their evolution since $z = 2$. We do not consider galaxies which may have had BPs at earlier epochs but do not at $z = 0$. To ensure enough stellar particles for our study, we analyse galaxies with $\log(M_*/M_\odot) \geq 10.0$. The methods used to find disc galaxies, those with bars at $z = 0$ and those barred galaxies with BPs at $z = 0$, are all described in detail in Appendix A. Briefly, our initial sample consists of 608 disc galaxies. We analyse only bars with radius ≥ 2.6 kpc, justifying this in Appendix A4.2. To compare with galaxies without BPs, we construct a sample of ‘control’ galaxies from the barred non-BP sample. We match a non-BP galaxy to a BP galaxy by stellar mass, with replacement (*i.e.* the control galaxy can be matched again with another BP), producing the ‘Control’ sample. We denote those BP galaxies which experienced strong buckling as the ‘BCK’ sample, and those which experienced weak or no buckling as the ‘WNB’ sample. The method used to differentiate between these classifications is described in Appendix A4.1.

¹<https://www.tng-project.org>

Table 1. Summary of notation used in the paper.

Symbol	Description
R_{eff}	Cylindrical radius containing half the total stellar mass
M_*	Stellar mass of a galaxy (within $r \leq 10R_{\text{eff}}$)
M_g	Gas mass of a galaxy (within $r \leq 10R_{\text{eff}}$)
$a_{2,\text{max}}$	Bar strength, calculated as described in Appendix A1
A_{bar}	Global bar strength (within $r \leq 10R_{\text{eff}}$), calculated via the $m = 2$ Fourier amplitude, as described in Appendix A1
R_{bar}	Bar radial extent, calculated as described in Appendix A1
f_g	The fraction of baryonic mass in gas, $M_g/(M_* + M_g)$
f_g, inbar	The fraction of baryonic mass in gas within the cylindrical radius R_{bar}
K_{rot}	Measure of the fraction of kinetic energy attributed to rotational motion, defined in Appendix A1
z_{rms}	The root mean square mass-weighted height (computed within $R_{\text{eff}} < R < 2R_{\text{eff}}$)
$\sigma_R, \sigma_\phi, \sigma_z$	The dispersion in the radial, azimuthal, and vertical velocities (within $r < 10R_{\text{eff}}$)
\mathcal{B}	‘Strength’ of the BP bulge, measured as described in Appendix A4
f_{acc}	Fractional accreted stellar mass of a galaxy. A stellar particle is considered to have been formed in situ if the galaxy in which it formed lies along the main progenitor branch (in the merger trees) of the galaxy in which it is currently found. Otherwise, it is tagged as ex situ, i.e. accreted (Rodríguez-Gómez et al. 2015)
\mathcal{F}	$M_{\text{gal}}(z)/M_{\text{group}}(z)$, where $M_{\text{gal}}(z)$ is the total mass of the galaxy (dark matter + gas and stars), and $M_{\text{group}}(z)$ is the total mass of the friends of friends group in which the galaxy is located at each redshift z
$t_{\text{bar}}(z_{\text{bar}})$	Time (redshift) of bar formation, assessed as described in Appendix A2
$t_{\text{BP}}(z_{\text{BP}})$	Time (redshift) of BP formation, assessed as described in Appendix A7
$t_{\text{buck}}(z_{\text{buck}})$	Time (redshift) of buckling, assessed as described in Appendix A4.1
$t_{1/2}(z_{1/2})$	Time (redshift) at which the galaxy’s stellar mass (within a sphere of radius $10R_{\text{eff}}$) reaches half its value at $z = 0$
V_c	The circular velocity at a cylindrical radius of $2R_{\text{eff}}$
M_T	The transition mass in the BP fraction, where the fraction reaches 50 per cent of its asymptotic value at high mass

For the reader’s convenience, a list of the notation we use for parameters of the galaxies is given in Table 1. Most are calculated within a sphere of radius $10R_{\text{eff}}$. However, heights are computed within a cylindrical annulus spanning $R_{\text{eff}} < R < 2R_{\text{eff}}$ so that we avoid the centre and any warping in the outer disc, although this does not always completely exclude the entire bar radius. This gives a fair comparison between those galaxies destined to host BPs, and those destined not to. The reader interested only in our results can consult Table 1 and skip Appendix A.

3 BP FREQUENCY AT REDSHIFT ZERO

From our sample of 608 disc galaxies with $\log(M_*/M_\odot) \geq 10.0$, we find 191 (32 per cent) have bars with $R_{\text{bar}} \geq 2.6$ kpc at $z = 0$ (Appendix A1), which is the ‘barred sample’. Of these, 106 (55 per cent) have BPs at $z = 0$ (the ‘BP sample’). In the BP sample, 52 (49 per cent) have strongly buckled in the past and 54 (51 per cent) have never strongly buckled. We find one galaxy (ID 608386) which appears to be in the process of buckling at $z = 0$. For this work

Table 2. Sample sizes of TNG50 galaxy classifications.

Classification	Number
Disc galaxies	608
Barred galaxies ($R_{\text{bar}} \geq 2.6$ kpc)	191
BP galaxies	106
Strongly buckling galaxies (BCK)	52
Weak/non-buckling galaxies (WNB)	54

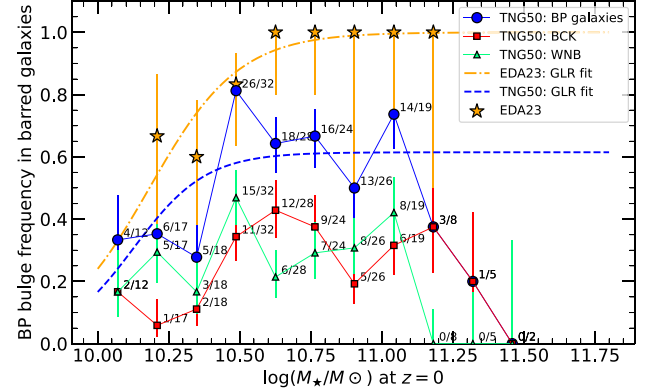


Figure 1. Dependence of the BP fraction on stellar mass at $z = 0$ for the sample of 191 barred galaxies (solid blue). It is split into the BCK (red) and WNB (green) populations. The fractions next to each point show the number of BP galaxies/number of barred galaxies in each mass bin. The blue dashed line represents a generalized logistic regression (GLR) fit to the data for all TNG50 BPs (see the text for details). The orange stars and dot dashed line represent the logistic regression fit to the observational data of EDA23 (restricted to bars of radius ≥ 2.6 kpc to match our selection, and limited to the same mass range as in this paper’s barred sample). Error bars are the 68 percent (1σ) confidence limits from the Wilson (1927) binomial confidence interval. TNG50 appears to significantly under-produce BP bulges, particularly at higher mass.

we consider this galaxy to be a non-BP galaxy but we reject it as a control (Appendix A5 describes how BP galaxies are assigned controls). Although not the focus of this study, we find five galaxies that appear to have buckled but do not have a BP at $z = 0$, and another two galaxies which did not buckle strongly, but had a BP that is no longer discernible by $z = 0$. A detailed analysis of these galaxies is outside the scope of this study. We summarize these statistics in Table 2.

Fig. 1 shows the variation of the BP fraction amongst barred galaxies (f_{BP}) as a function of stellar mass at $z = 0$ in TNG50. ED17 found an increasing f_{BP} with M_* (see their fig. 5) from an analysis of 84 local barred galaxies in the S⁴G catalogue (Sheth et al. 2010). We also show results from EDA23 which uses a larger data set (132 galaxies) from a distance-limited subset of S⁴G, using *Spitzer* 3.6-micron images. From the EDA23 sample, we exclude bars with radii < 2.6 kpc and restrict the mass range to our TNG50 barred sample. This cut results in 27 galaxies, 23 of which (85 per cent) have BPs.

At low mass ($\log(M_*/M_\odot) \sim 10.1$), the BP fraction in TNG50 is low, similar to the results of ED17. In TNG50, f_{BP} increases rapidly for increasing M_* until the fraction reaches ~ 0.6 at $\log(M_*/M_\odot) \sim 10.5$, followed by a plateau at higher masses. TNG50 does not match the observed BP fraction for $\log(M_*/M_\odot) \gtrsim 10.6$. All the galaxies with $\log(M_*/M_\odot) \gtrsim 11.2$ in the sample of ED17, and all the galaxies with $\log(M_*/M_\odot) \gtrsim 10.6$ in EDA23, have BPs.

Table 3. Generalized logistic regression fit to f_{BP} as a function of $\mu = \log(M_*/M_\odot)$ at $z = 0$, with 1σ errors from bootstrap resampling. The functional form fitted is a generalized logistic regression function of the form $f_{\text{BP}}(\mu) = K/[1 + \exp(-(\alpha + \beta\mu))]$. M_T is the transition mass where f_{BP} reaches half of the asymptotic fraction at high mass (K). We show the generalized fits for all BP galaxies, BCK and WNB samples. The last row shows the logistic regression fits for the EDA23 data, with $\log(M_*/M_\odot)$ and R_{bar} cuts to match those in this study.

Sample	K	α	β	$\log(M_T/M_\odot)$
All BPs	0.61 ± 0.05	-79.48 ± 17.93	7.85 ± 1.70	10.13 ± 0.07
BCK	0.33 ± 0.05	-68.50 ± 24.96	6.69 ± 2.35	10.25 ± 0.18
WNB	0.30 ± 0.04	-99.08 ± 31.66	9.86 ± 2.40	10.06 ± 0.06
EDA23	1.00 ± 0.00	-64.43 ± 24.73	6.33 ± 2.30	10.19 ± 0.06

Following ED17, we quantify the mass dependence of the BP fraction using logistic regression, which models whether a barred galaxy has a BP or not, with a function for the probability of a binomial property. We generalize the fitted function to account for the fact that at higher mass, f_{BP} does not asymptote to 1 in TNG50:

$$P(\mu) = \frac{K}{1 + e^{-(\alpha + \beta\mu)}}, \quad (1)$$

where $\mu \equiv \log(M_*/M_\odot)$ (or other variable being fitted) and K is the asymptotic fraction of BPs at high mass. β is the steepness of the curve, the rate at which the probability increases or decreases with μ . The ratio $-\alpha/\beta$ is the midpoint of the curve, i.e. the value of μ where $P(\mu)$ reaches $K/2$.

The procedure fits all data points (i.e. ‘has BP? Y/N’ indicator versus $\log(M_*/M_\odot)$ points for all 191 barred galaxies), not the binned data. The parameters of the fit² are shown in Table 3, and the fit is presented in Fig. 1 (dashed blue line). In TNG50 the ‘transition mass’ M_T , where f_{BP} reaches 50 percent of the asymptotic fraction K , is $\log(M_T/M_\odot) = 10.13 \pm 0.07$, which occurs at $f_{\text{BP}} \sim 0.31$. ED17 found a transition mass of $\log(M_T/M_\odot) \approx 10.37$ at $f_{\text{BP}} = 0.5$ (10.3–10.4 when they considered data from the edge-on galaxies of Yoshino & Yamauchi 2015). Note that stellar masses in ED17 were determined using estimated stellar M/L ratios, and so have some inherent uncertainty. The logistic regression for the EDA23 data set, which asymptotes to 1 at high mass, yields a transition mass of $\log(M_T/M_\odot) = 10.19 \pm 0.06$, a difference of just 0.06 dex from the TNG50 result.³

4 MULTIVARIABLE FITS

To discern the drivers behind the BP fraction in TNG50 we perform multiple generalized logistic regression fits to equation (1) with the following variables: R_{bar} , t_{bar} , $t_{1/2}$, $(\sigma_z/\sigma_R)_{\text{inbar}}$, $a_{2,\text{max}}$, $\log(M_*/M_\odot)$, f_{acc} , R_{eff} , $f_{\text{g, inbar}}$, z_{rms} , and $z_{\text{rms}}/R_{\text{eff}}$ (all defined in Table 1). We also perform the fit with pairs of these variables (μ_1, μ_2). In this case we fit:

$$P(\mu_1, \mu_2) = \frac{K}{1 + e^{-(\alpha + \beta_1\mu_1 + \beta_2\mu_2)}}, \quad (2)$$

where β_1 and β_2 are the steepness measures of the curve attributed to variables μ_1 and μ_2 , respectively.

²The fits were performed using the PYTHON SCIPY.OPTIMIZE library’s MINIMIZE function, with a Nelder–Mead solver.

³Excluding the R_{bar} cut from the EDA23 data, but retaining that in $\log(M_*/M_\odot)$ (48 galaxies) yields $\log(M_T/M_\odot) = 10.31 \pm 0.06$.

Table 4. Generalized logistic regression fits to f_{BP} and AIC_c as a function of a variety of variables at $z = 0$, for the barred sample.

Variable ($z = 0$)	K	α	β	AIC_c
R_{bar}	1.0	−6.18	1.78	192.86
$(\sigma_z/\sigma_R)_{\text{inbar}}$	1.0	18.15	−23.37	215.38
$a_{2,\text{max}}$	1.0	−3.44	9.45	234.52
$t_{1/2}$	0.69	10.16	−1.29	247.9
f_{acc}	0.63	5.11	−18.05	252.59
t_{bar}	0.64	6.61	−0.58	255.83
M_*	0.61	−79.48	7.85	261.08
$z_{\text{rms}}/R_{\text{eff}}$	1.0	1.52	−1.88	261.35
f_{g}	0.59	11.28	−20.0	261.38
z_{rms}	1.0	0.77	−0.17	264.22
$f_{\text{g, inbar}}$	0.56	635.63	−5000.0	264.88
R_{eff}	0.58	−0.67	1.17	267.41

Table 5. Generalized logistic regression fits to f_{BP} and AIC_c as a function of combinations of two variables at $z = 0$, one of which is R_{bar} , for the barred sample. β_1 applies to R_{bar} , β_2 to the second variable.

Variables ($z = 0$)	K	α	β_1	β_2	AIC_c
$R_{\text{bar}}, (\sigma_z/\sigma_R)_{\text{inbar}}$	1.00	10.43	1.51	−20.44	166.05
$R_{\text{bar}}, a_{2,\text{max}}$	1.00	−9.92	1.62	10.89	168.08
$R_{\text{bar}}, z_{\text{rms}}/R_{\text{eff}}$	1.00	−4.74	1.85	−2.45	186.89
$R_{\text{bar}}, t_{\text{bar}}$	1.00	−5.14	1.75	−0.14	190.44
$R_{\text{bar}}, f_{\text{g, inbar}}$	1.00	−5.93	1.77	−11.88	191.01
$R_{\text{bar}}, f_{\text{acc}}$	1.00	−5.57	1.71	−3.28	191.33
$R_{\text{bar}}, t_{1/2}$	1.00	−5.01	1.69	−0.13	193.83
$R_{\text{bar}}, f_{\text{g}}$	1.00	−6.60	1.84	0.81	194.44
R_{bar}, M_*	1.00	−3.04	1.79	−0.30	194.64
$R_{\text{bar}}, R_{\text{eff}}$	1.00	−6.34	1.79	0.02	194.82
$R_{\text{bar}}, z_{\text{rms}}$	0.73	−12.67	3.33	1.00	242.97

We assess the power of each variable (and combination of variables) to explain the variation of BP fraction using the Akaike Information Criteria (AIC) (Akaike 1974), which gives us a basis for comparison.⁴ AIC compares different models’ abilities to explain the greatest amount of variation in the data. We use AIC_c , the AIC corrected for small sample sizes, which is given by $\text{AIC}_c = \text{AIC} + 2k(k+1)/(N-k-1)$ (Sugiura 1978). In our case, the number of data points is $N = 191$, so the correction is small. We change variable μ in equation (1) (and combinations of variables μ_1, μ_2 in equation 2), and for each variable/combination of variables, compute the AIC_c . The lower the value of the AIC_c , the greater the power of that variable/combination of variables to ‘explain’ whether a galaxy hosts a BP. Differences between fits of $|\Delta\text{AIC}_c| > 6$ are considered strong evidence in favour of the model with lower AIC_c (ED17). Results are shown in Tables 4 and 5.

Table 4 shows that as a single variable, R_{bar} has the greatest explanatory power for f_{BP} , rather than M_* . Table 5 shows the results of combinations of R_{bar} with other variables. The combinations of R_{bar} with $(\sigma_z/\sigma_R)_{\text{inbar}}$ and $a_{2,\text{max}}$ have the lowest AIC_c , fully ~ 26 lower than for R_{bar} alone. $(\sigma_z/\sigma_R)_{\text{inbar}}$ is key to the buckling instability, reaching low values before buckling occurs; in this sense it is an inverse proxy for bar strength. We discuss this further in Section 5.2. We also assessed combinations of R_{bar} and $(\sigma_z/\sigma_R)_{\text{inbar}}$ with a third variable, and found that the combinations of R_{bar} ,

⁴The AIC for a model is defined as $2k - 2\ln\mathcal{L}_{\text{max}}$, where \mathcal{L}_{max} is the maximized likelihood of the model, and k is the number of parameters in the model.

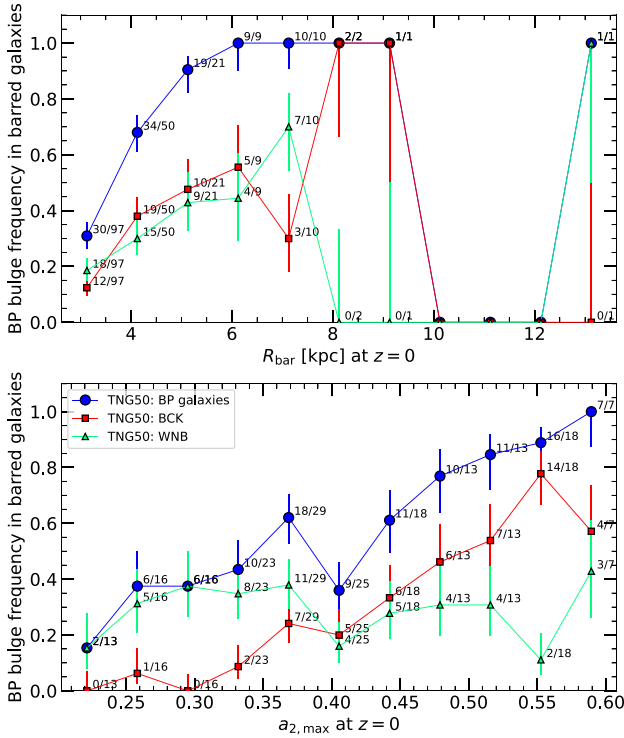


Figure 2. Dependence of the BP fraction on R_{bar} (top panel) and $a_{2,\text{max}}$ (lower panel) at $z = 0$ for the sample of 191 barred galaxies (solid blue). It is split into the BCK (red) and WNB (green) populations. The fractions next to each point show the number of BP galaxies/number of barred galaxies in each mass bin. Error bars are the 68 percent (1σ) confidence limits from the Wilson (1927) binomial confidence interval. The BP fraction in TNG50 is highly dependent on these bar parameters.

$(\sigma_z/\sigma_R)_{\text{inbar}}$ and $a_{2,\text{max}}$ gave a slightly lower AIC_c but this was not significant ($\Delta\text{AIC}_c \sim -1$). We conclude that the probability of a bar hosting a BP is a function of bar length and bar strength in TNG50. We show f_{BP} as a function of R_{bar} and $a_{2,\text{max}}$ in Fig. 2. This clearly shows the strong dependence of BP fraction on both bar parameters – the stronger, and the longer the bars, the greater the fraction of them which host BPs.

Whereas observations find that f_{BP} can be fully accounted for by $\log(M_*/M_\odot)$ (ED17, also EDA23 who looked at bar strength and found no evidence of an effect), in TNG50 $\log(M_*/M_\odot)$ has relatively poor explanatory power among the variables we have examined. We discuss this disagreement in Section 8.

5 THE KINEMATIC STATE OF BP PROGENITORS

The dependence of f_{BP} on galaxy properties in TNG50 barred galaxies motivates us to understand the evolutionary differences between BP and non-BP barred galaxies. We begin by examining their evolution, showing their median properties at each redshift. Whilst there is variation in the properties for any sample of galaxies, by comparing the medians between different subsamples with the same mass distribution, we can identify key differences in their evolutionary histories. In the following plots, we show the medians and the 95 percent confidence intervals about the median (from bootstrap resampling) to highlight trends. We stress that the underlying distributions have significant scatter.

5.1 Bar size and strength

We plot the evolution of the bar strength and radius in Fig. 3. This shows that the BP sample has had, since $z \sim 1$, stronger bars on average than the non-BP bars. By $z = 0$, BP bars are ~ 22 per cent stronger than those in the controls. At $z = 0$, the median bar radius for the BP sample is 4.1 kpc, while for the controls it is 3.0 kpc. As a fraction of the effective radius, the median $R_{\text{bar}}/R_{\text{eff}}$ is 1.1 for BP galaxies, but only 0.66 for the controls, with two-sample Kolmogorov–Smirnov (KS) tests confirming a significant difference in distributions at $z = 0$. Thus BPs are found in relatively (and in absolute terms) stronger and longer bars at $z = 0$ compared to the bars in the non-BP galaxies. We have checked that there is no monotonic relation between R_{bar} and stellar mass for BCK, WNB or non-BP galaxies at $z = 0$, at least for our sample with $R_{\text{bar}} \geq 2.6$ kpc (Spearman $\rho \lesssim 0.2$). This is consistent with Zhao et al. (2020), who found that the bar length/stellar mass relation flattens around $\log(M_*/M_\odot) \sim 10.7$ in TNG100. For $R_{\text{bar}}/R_{\text{eff}}$ however, there is a decrease with stellar mass for each subgroup, since R_{eff} increases with mass. None the less as Fig. 3 shows, the finding of BPs being hosted in relatively longer bars holds even when controlling for mass (controls and non-BP galaxies show a similar median value of $R_{\text{bar}}/R_{\text{eff}}$ below that of the BPs).

Fig. 4 shows f_{BP} split at the $z = 0$ median bar length ($R_{\text{bar}} = 3.5$ kpc top panel), median $(\sigma_z/\sigma_R)_{\text{inbar}}$ (middle panel) and median bar strength ($a_{2,\text{max}} = 0.39$ bottom panel). The denominator in f_{BP} in this plot in each mass bin is the total number of barred galaxies within the population of short/weak (olive line) and long/strong (orange dashed line) bars. The figure clearly shows a preference, at almost all masses, for BPs to be found in galaxies with longer and stronger bars and lower $(\sigma_z/\sigma_R)_{\text{inbar}}$, consistent with these variables having the lowest AIC_c . As we shall see, however, just because a variable’s evolution is different for BPs and non-BPs does not necessarily mean that it will have a low AIC_c .

5.2 Kinematics and thickness

We now compare the kinematics of the BP galaxies with those of the controls. Fig. 5 presents the evolution of velocity dispersions (normalized by the circular velocity at $2R_{\text{eff}}$) $\sigma_{z,\text{inbar}}/V_c$, $\sigma_{R,\text{inbar}}/V_c$, and the ratio $(\sigma_z/\sigma_R)_{\text{inbar}}$ (all within the bar). We focus on the bar region given our previous findings. In the BP galaxies, both $\sigma_{z,\text{inbar}}/V_c$ and $\sigma_{R,\text{inbar}}/V_c$ rise steadily until the current epoch with $\sigma_{R,\text{inbar}}/V_c$ perhaps rising faster. In the non-BP galaxies, $\sigma_{R,\text{inbar}}/V_c$ flattens from $z \sim 0.5$.

The overall effect is seen in the ratio $(\sigma_z/\sigma_R)_{\text{inbar}}$, which is key to the buckling instability, because it needs to reach low values (the bar becomes highly radially anisotropic) before buckling occurs (Toomre 1966; Raha et al. 1991; Sellwood 1996). $(\sigma_z/\sigma_R)_{\text{inbar}}$ declines steadily in the BP galaxies from $z \sim 1$, reaching a value of ~ 0.75 at $z = 0$. BP galaxies become more radially anisotropic as their bars strengthen, $\sigma_{R,\text{inbar}}/V_c$ grows and σ_z/σ_R declines. Eventually in the BCK sample, buckling is triggered (Sellwood 1996). In the controls the decline is halted after $z \sim 1$ (even increasing slightly). Their bars fail to strengthen significantly after this epoch, as seen in $a_{2,\text{max}}$ (Fig. 3, upper left panel).

In Fig. 6, we show the evolution of the velocity dispersions within the bar, but this time around t_{buck} . The plot shows that, in contrast to isolated simulations (e.g. Sotnikova & Rodionov 2003; Martinez-Valpuesta & Shlosman 2004; Martinez-Valpuesta, Shlosman & Heller 2006; Rodionov & Sotnikova 2013; Khoperskov & Bertin 2017; Łokas 2019; Li et al. 2023), on average $(\sigma_z/\sigma_R)_{\text{inbar}}$ remains

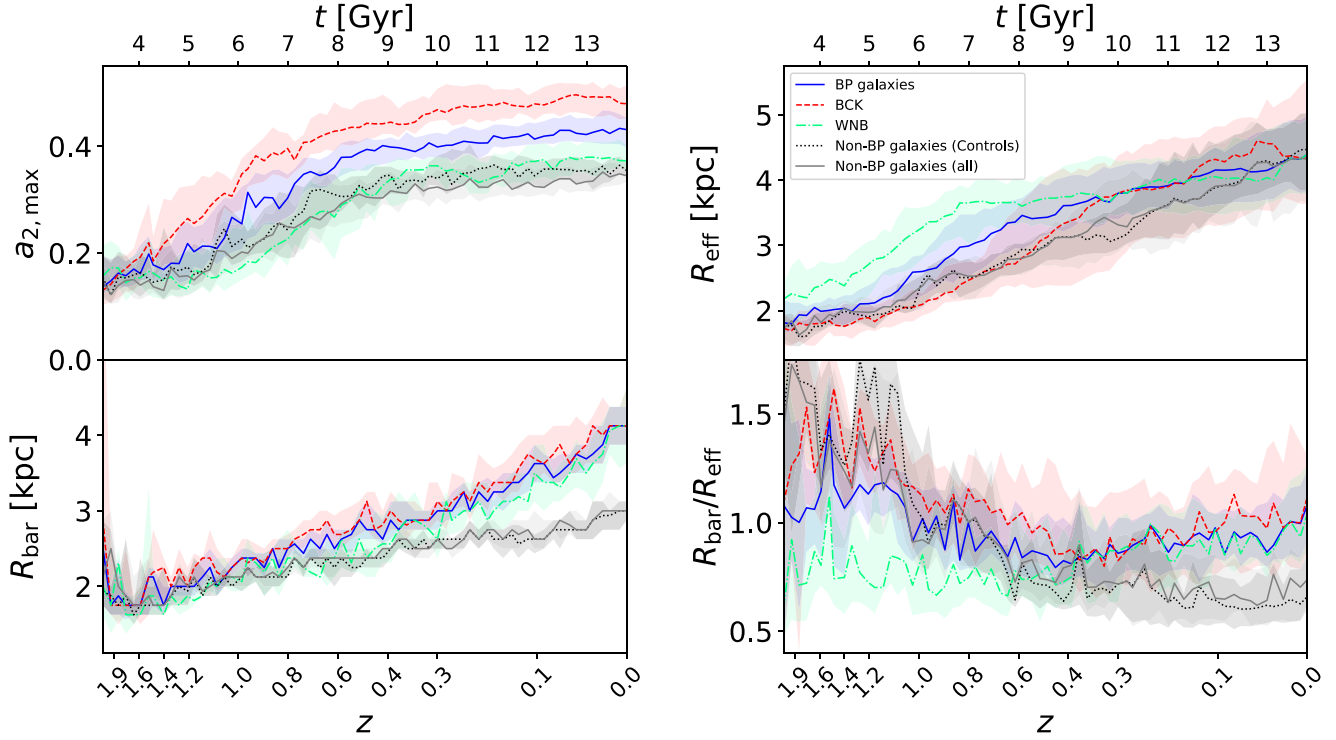


Figure 3. Evolution of the median bar strength (as measured by $a_{2,\max}$), R_{bar} , R_{eff} , and $R_{\text{bar}}/R_{\text{eff}}$ for BP, BCK, WNB, non-BP bars, and controls. The shaded areas represent the 95 per cent confidence interval about the median from bootstrap resampling.

rather flat after buckling. This implies that the ratio likely falls (or remains flat) for some galaxies after buckling. We have investigated this behaviour for a number of BCK galaxies, and found that the ratio was lower 2 Gyr after buckling in 22 of 52 BCK galaxies (the ‘fallers’). In almost all BCK galaxies, σ_z rises after buckling then flattens, but for the fallers, σ_R also rises through buckling and continues to do so, resulting in the ratio falling. In these galaxies, the bar strength continues to rise after buckling, somewhat unintuitively.

We explore whether this behaviour arises because some populations are immune to buckling by examining the evolution of the velocity dispersions in bins of time of formation, t_{form} ; we find large populations of stars within the fallers (and in those where the ratio remains flat) seemingly unaffected by buckling, as evidenced by the behaviour of σ_z and σ_R around t_{buck} . We compute the fraction of the stellar population which buckles in a simple way. For each group of stellar particles in bins of t_{form} , we calculate the fractional change in σ_z from $t_{\text{buck}} - 0.5$ Gyr to $t_{\text{buck}} + 1.5$ Gyr (to avoid noise around buckling itself), $f_{\Delta\sigma_z}$. If the t_{form} bin has $f_{\Delta\sigma_z} > 0.1$, we deem the population to have buckled. Hence for each galaxy we calculate the overall fraction of stars which have buckled (f_{buck}). We find that the lower f_{buck} , the smaller the rise in $(\sigma_z/\sigma_R)_{\text{inbar}}$. Thus, our analysis suggests that the reason the median value of $(\sigma_z/\sigma_R)_{\text{inbar}}$ remains flat after buckling is that there are a significant number of buckling galaxies which host a stellar population sufficiently hot to resist buckling.

Fig. 5 also shows that non-BPs have higher $\sigma_{z,\text{inbar}}/V_c$ or much of their evolution, hinting they may have been thicker (the control sample is controlled for stellar mass by design, so this is not a mass effect). Fig. 7 (upper panel) shows the evolution of the mass-weighted root-mean-square height (z_{rms}). For this plot, we compute

z_{rms} and $z_{\text{rms}}/R_{\text{eff}}$ within $R_{\text{eff}} < R < 2R_{\text{eff}}$, and so mainly in the disc region. On average, the BP galaxies have somewhat lower disc heights than the controls, especially after $z \sim 0.4$, although the difference is not significant. Normalized by the effective radius (lower panel), the BP galaxies are thinner at $z = 0$, and have been throughout their history. Controls and non-BP bars show similar evolution, so the trends found hold even when controlling for mass.

Thus, while BP galaxy discs have similar heights on average as non-BPs at $z = 0$, normalized by their host galaxy size they have been thinner than non-BPs for most of their evolution down to $z = 0$.

5.3 Impact of mergers on the evolution of the samples

Mergers can heat galaxies (e.g. Quinn, Hernquist & Fullagar 1993; Reshetnikov & Combes 1996, 1997; Sellwood, Nelson & Tremaine 1998; Purcell, Bullock & Kaplinghat 2009; Qu et al. 2011, and references therein) and weaken bars (e.g. Ghosh et al. 2021). We explore the impact of merger and accretion events on the evolution of BPs. Fig. 8 shows the median accreted stellar mass fraction, f_{acc} . The figure reveals a divergence in behaviour between BP galaxies and non-BPs starting at $z \sim 1$, after which the BP galaxies’ accreted fraction remains constant. In contrast, for the controls, f_{acc} rises continually after this point (and their vertical heating is significantly higher throughout their history). Furthermore, the median time of the last major merger (mass ratio larger than 1/10), is $z = 0.89$ for the controls, but $z = 1.41$ for the BPs, fully 1.85 Gyr earlier. Major merger activity for BPs ends much earlier than for the controls.

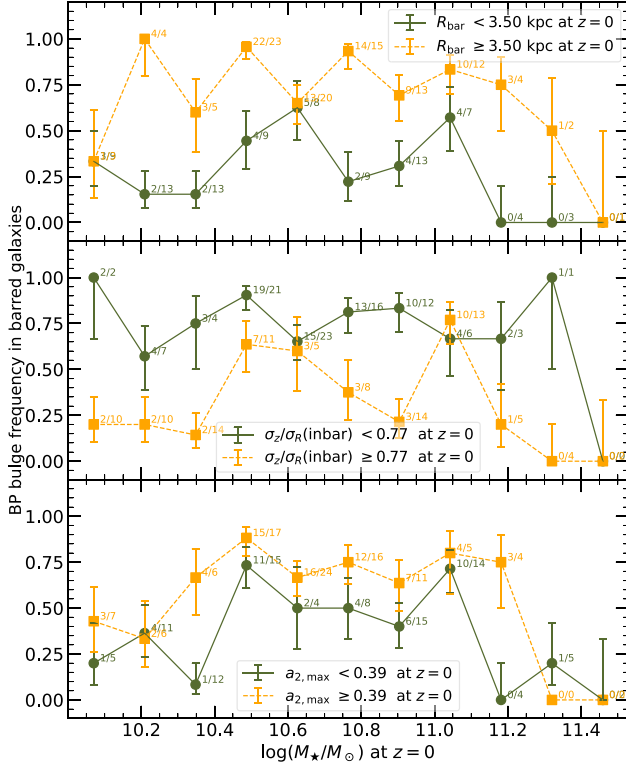


Figure 4. The fraction of barred galaxies hosting BPs at $z = 0$, split into high (orange dashed line, squares) and low (olive solid line, circles) populations by median R_{bar} (upper panel), median $(\sigma_z/\sigma_R)_{\text{inbar}}$ (middle panel) and median $a_{2,\text{max}}$ (lower panel). At almost all masses, BPs are hosted preferentially in galaxies whose bars are longer and stronger than the median, and for which $(\sigma_z/\sigma_R)_{\text{inbar}}$ is lower than the median. Error bars are the 68 percent (1σ) confidence limits from the Wilson (1927) binomial confidence interval.

The epoch of this divergence in f_{acc} coincides with the growth in bar length and strength, and stall in the decrease in σ_z/σ_R in the non-BPs (Sections 5.1 and 5.2). It also coincides with the time at which the disc’s vertical and radial cooling stall in the controls (Fig. 5). We find $f_{\text{acc}} = 6.3$ per cent at $z = 0$ for BP galaxies, but 10.0 per cent for non-BP and control galaxies. Although the AIC_c for f_{acc} is higher than for bar length and strength (and so has a weaker discriminatory power as to whether a galaxy hosts a BP), these results imply that a sufficiently high accreted fraction suppresses BP formation by hindering the growth of a bar.

In TNG50, it may be that the heating of the disc prevents the controls’ bars from strengthening, and that the accumulation of a satellite’s mass in the central region of the host (e.g. Ghosh et al. 2021) weakens the bars after $z \sim 1$. Mergers heat discs in all directions (Quinn, Hernquist & Fullagar 1993), so the large exposure to mergers in the controls and non-BPs holds $(\sigma_z/\sigma_R)_{\text{inbar}}$ approximately constant on average, rather than declining as occurs in the BP bars.

We have checked Spearman rank correlations at $z = 0$ and find a significant correlation between f_{acc} and z_{rms} for both BP and non-BP samples ($\rho \sim 0.8$, $p \lesssim 10^{-23}$), and between f_{acc} and R_{eff} ($\rho \sim 0.7$, $p \lesssim 10^{-15}$). These results support the notion that merger activity influences a galaxy both vertically and radially, but that height may be impacted more, resulting in control and non-BP galaxies’ higher

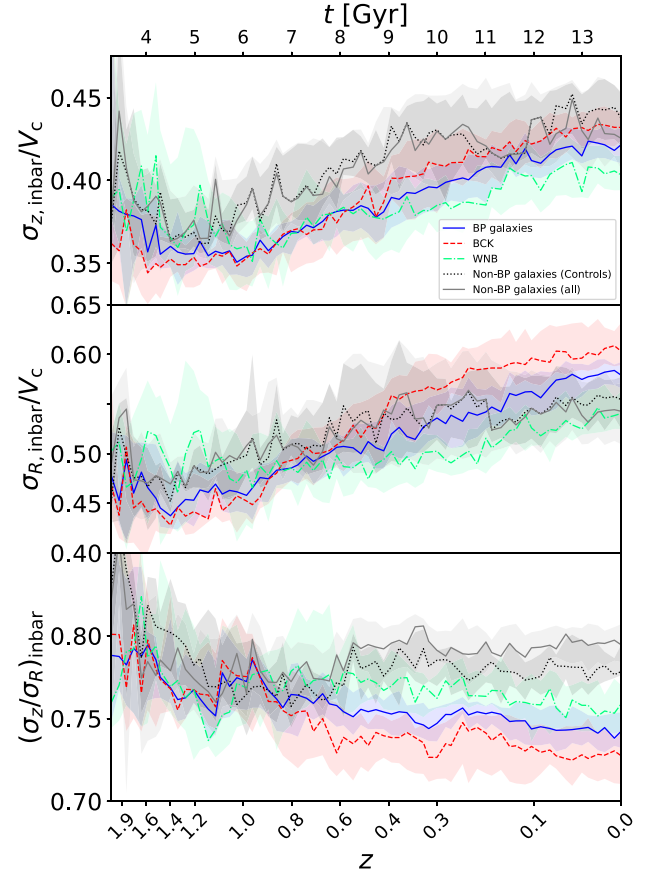


Figure 5. Evolution of the median $\sigma_{z,\text{inbar}}/V_c$ (upper), $\sigma_{R,\text{inbar}}/V_c$ (middle), and $(\sigma_z/\sigma_R)_{\text{inbar}}$ (lower) ratios, for BP, BCK, WNB, non-BP bars and controls. The shaded areas represent the 95 percent confidence interval about the median from bootstrap resampling.

relative heights. We also find a negative correlation between f_{acc} and $a_{2,\text{max}}$, which we discuss in Section 8.

We also explore whether environment plays any role in BP formation. Of the 608 disc galaxies, 413 (68 per cent) are centrals and 195 (32 per cent) are satellites. Of the 191 barred galaxies, 130 (68 per cent) are centrals and 61 (32 per cent) are satellites. Of the 106 BP galaxies amongst those bars, 77 (73 per cent) are centrals and 29 (27 per cent) are satellites. These $z = 0$ fractions are consistent, hinting that a galaxy’s classification as a central or satellite is not relevant to whether it hosts a BP.

We compute $\mathcal{F} = M_{\text{gal}}(z)/M_{\text{group}}(z)$, where $M_{\text{gal}}(z)$ is the total mass of the galaxy (dark matter + gas + stars) within $10R_{\text{eff}}$, and $M_{\text{group}}(z)$ is the total mass (dark matter + gas + stars) of the friends of friends group in which the galaxy is located (supplied as part of the IllustrisTNG public data release), at each z . We expect galaxies with small \mathcal{F} to be more influenced by tidal effects than galaxies with large \mathcal{F} . If environment plays a major role in determining whether a galaxy forms a BP, we expect a difference in \mathcal{F} between BPs and non-BPs. We show the evolution of median \mathcal{F} in Fig. 9. Although \mathcal{F} is systematically somewhat lower for non-BPs (dashed lines) than BPs (solid lines), it is not statistically significant except perhaps for $z > 0.5$ for satellites. We conclude that whether a galaxy is a satellite or central, the BP and non-BP galaxies share *approximately* the same \mathcal{F} , but with controls having somewhat lower values on average.

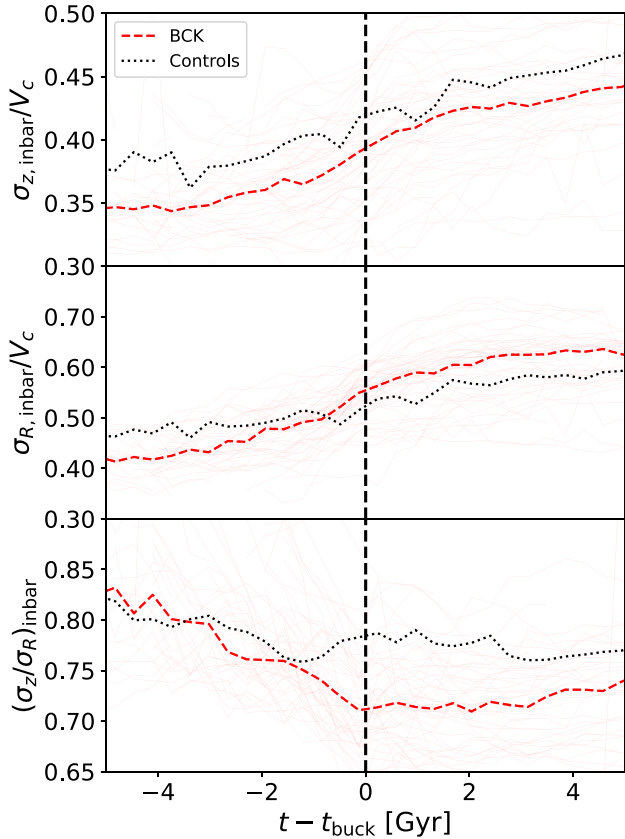


Figure 6. Evolution of the median $\sigma_{z,\text{inbar}}$ (upper), $\sigma_{R,\text{inbar}}$ (middle), $(\sigma_z/\sigma_R)_{\text{inbar}}$ (lower) around the time of buckling t_{buck} , for BCK (red dashed line) and control (black dotted line) galaxies. $\sigma_{z,\text{inbar}}$ and $\sigma_{R,\text{inbar}}$ are normalized by the circular velocity at $2R_{\text{eff}}$. We show bins in $t - t_{\text{buck}}$ containing 10 galaxies or more. We show individual BCK galaxies with thin red lines. The median $(\sigma_z/\sigma_R)_{\text{inbar}}$ remains rather flat after buckling.

The AIC_c for \mathcal{F} , is 266.48, 13.9 higher than for f_{acc} (Table 3). So environment matters only indirectly, via its legacy in f_{acc} in determining the probability of hosting a BP. We conclude that merger activity as measured by f_{acc} is a significant contributor to non-BP galaxies’ relatively thicker discs and weaker bars, and the suppression of BP formation.

6 DOWNSIZING AND BAR/BP AGE

Fig. 10 shows the cumulative distribution of the time at which each galaxy assembles half of its $z = 0$ stellar mass ($t_{1/2}$). On average, BP galaxies assemble their stellar mass ~ 1 Gyr earlier than the controls. The figure also shows the times of bar and BP formation (t_{bar} and t_{BP} , respectively) and times of buckling. It shows that bars in the BP galaxies form ~ 2 Gyr earlier on average than those in the controls. Bars in BCK galaxies form ~ 2 Gyr earlier than those in WNBs, even though there is no statistically significant difference in their mass distribution. Thus BP bars are on average older than non-BP bars, and bars in strongly buckled galaxies are on average older than in WNB and non-BP barred galaxies. Thus a ‘sequence’ of bar age, young to old (controls \rightarrow WNB \rightarrow BCK), exists. Clearly galaxy mass assembly and bar formation time-scales influence BP formation. This motivates us to further compare old and young bars. We note in passing that the bottom panels of Fig. 10 show that the BP formation and buckling rates are consistent with being constant with

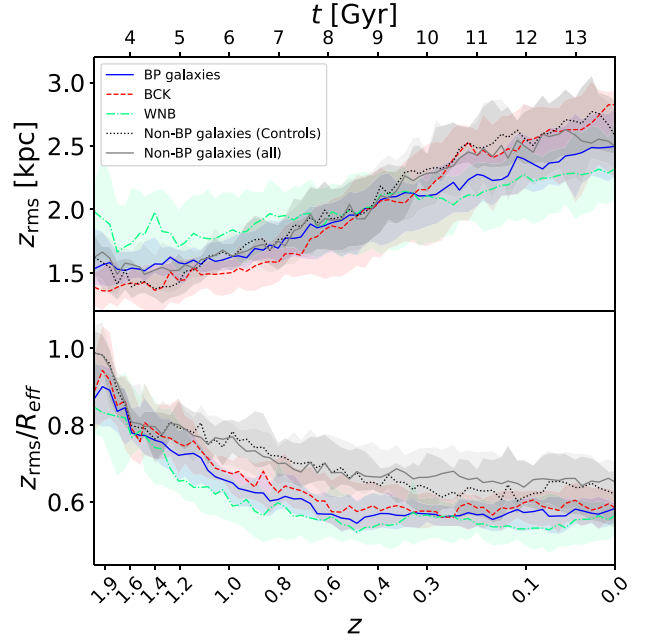


Figure 7. Evolution of the median z_{rms} and $z_{\text{rms}}/R_{\text{eff}}$ for BP, BCK, WNB, control and non-BP galaxies. z_{rms} is computed within $R_{\text{eff}} < R < 2R_{\text{eff}}$, therefore mainly in the disc region. The shaded areas represent the 95 per cent confidence interval about the median from bootstrap resampling. BPs occur in relatively somewhat thinner discs than non-BPs.

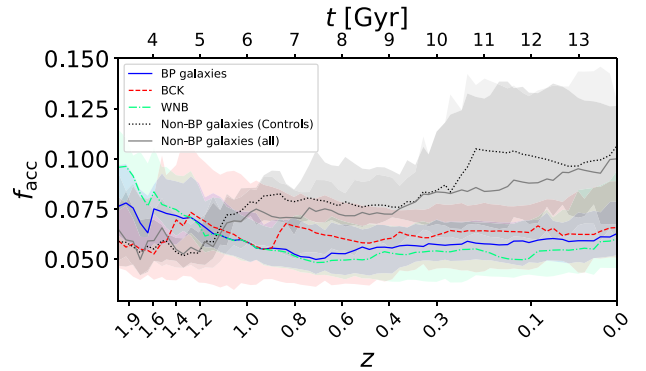


Figure 8. Evolution of the median accreted stellar mass fraction f_{acc} for BP, BCK, WNB, controls and non-BP barred galaxies. The shaded areas represent the 95 per cent confidence interval about the median from bootstrap resampling.

time, albeit with the caveat that we only examine those BPs extant at $z = 0$. Furthermore, the lower left panel showing t_{BP} is in reasonable agreement with Kruk et al. (2019), who estimated the earliest BPs to form at $z \sim 1$ (note that their work examined BPs at those earlier redshifts, whereas this study examines only $z = 0$ BPs).

Fig. 11 shows individual galaxies as points on three 2D planes at $z = 0$. The left panel (the $(t_{\text{bar}}, R_{\text{bar}})$ -plane) shows that for the non-BP galaxies, bars are relatively short irrespective of their age. For BP galaxies, in contrast, older BP bars tend to be longer. The panel also shows that at a given bar age, BPs are hosted in galaxies with larger bars. The middle panel of Fig. 11 (the $(t_{\text{bar}}, a_{2,\text{max}})$ -plane) shows that older bars (lower t_{bar}) are stronger than younger bars, contributing to the relative lack of BPs amongst younger bars.

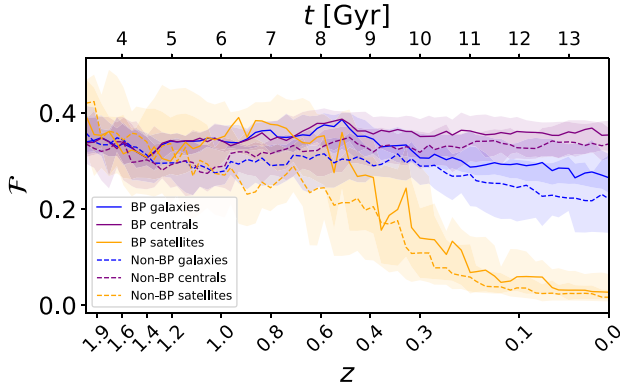


Figure 9. Evolution of the median $\mathcal{F} = M_{\text{gal}}(z)/M_{\text{group}}(z)$ for BPs and non-BPs. The shaded areas represent the 95 percent confidence interval about the median from bootstrap resampling. BPs and non-BPs (whether satellites or centrals) share approximately the same \mathcal{F} for most of their evolution.

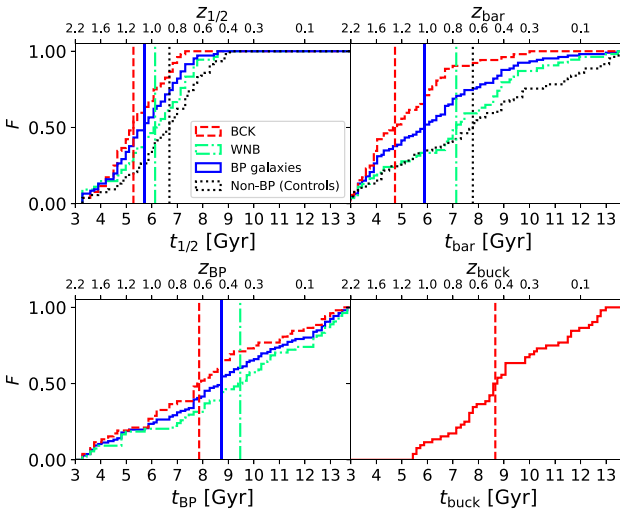


Figure 10. Cumulative distributions of the times by which the stellar mass of the samples reaches half its value at $z = 0$ ($t_{1/2}$) (top left panel), t_{bar} (top right panel), t_{BP} (lower left panel), and t_{buck} (lower right panel). Medians are shown as vertical dashed lines. Bars in BP galaxies form much earlier than those of the same stellar mass without BPs.

The right panel shows the $(\log(M_*/M_\odot), t_{\text{bar}})$ plane and reveals that the bars in high-mass galaxies formed earlier than those in low-mass galaxies. A similar trend was found in TNG100 by Rosas-Guevara et al. (2020). This ‘downsizing’ trend has been noted in observations by Sheth et al. (2008) and more recently by Cuomo et al. (2020). We have checked the correlation between t_{bar} and $t_{1/2}$, finding them to be monotonically related,⁵ albeit with some scatter. Therefore, this result seems to be driven by stellar downsizing, where the stars in more massive galaxies tend to have formed earlier (Neistein, van den Bosch & Dekel 2006; Pilyugin & Thuan 2011). At lower mass ($\log(M_*/M_\odot) \lesssim 10.3$) there are fewer BP galaxies compared to non-BP galaxies than at higher mass (Fig. 1). This is driven by the lack of *old* bars (low t_{bar}) at low mass, particularly BCK galaxies (a much weaker effect is also seen for WNB galaxies) – see the CDF at the top. This is confirmed in

Fig. 12, which shows $f_{\text{BP}}(M_*)$ split by the median t_{bar} for all barred galaxies (6.82 Gyr). Younger bars are less likely than older bars to host BPs.

So even though overall t_{bar} has a weaker discriminatory power as to whether a galaxy hosts a BP than R_{bar} (Table 4), none the less bar age plays a role in the emergence of a BP.

7 THE ROLE OF GAS

Simulations of isolated galaxies show that high gas content suppresses buckling (Berentzen et al. 1998; Debattista et al. 2006; Berentzen et al. 2007; Wozniak & Michel-Dansac 2009; Łokas 2020), whereas ED17 found no observational link between the presence of BP bulges and the global gas content (as measured by M_{HI}/M_*), after controlling for the dependence of gas fraction on stellar mass. These seemingly contradictory results motivate us to test for any role for gas in TNG50 BP bulge formation.

In the studies cited above, the gas fractions required to suppress buckling vary substantially.⁶ Amongst isolated simulations, Berentzen et al. (2007) found buckling was suppressed for $f_g \gtrsim 0.03$, Wozniak & Michel-Dansac (2009) found buckling suppressed for $f_g \sim 0.1$, and Łokas (2020) found that $f_g = 0.3$ was sufficient, with buckling occurring for $f_g = 0.2$. In TNG50 we find median $f_g \sim 0.4$ at t_{BP} , the fraction in the BCK sample being somewhat lower than that in the WNB and control samples.

Tables 4 and 5 show that neither f_g nor $f_{g,\text{inbar}}$ are able to discriminate between BPs and non-BPs significantly compared to bar length and strength (AIC_c for $f_{g,\text{inbar}}$ is fully 72.0 higher than for R_{bar}). Fig. 13 shows the evolution of $f_{g,\text{inbar}}$, also as a function of $\Delta t_{\text{bar}} = t - t_{\text{bar}}$ and $\Delta t_{\text{BP}} = t - t_{\text{BP}}$. In the left panel, we see no significant evolutionary differences between BP galaxies and controls.

At t_{bar} , $f_{g,\text{inbar}} \sim 0.07$ for BPs and controls. Since the difference at t_{bar} is insignificant, galaxies destined to host BPs are not sensitive to the gas fraction at the time their bars form. Likewise, at t_{BP} , $f_{g,\text{inbar}}$ is similar in BP galaxies and in the controls (~ 0.02). Two-sample KS tests confirm the lack of significant differences in the distributions of $f_{g,\text{inbar}}$ at t_{bar} and t_{BP} for BPs and controls ($p \sim 0.06$ and 0.02 , respectively). It seems that the gas fraction within the bar does not significantly inhibit the formation of BPs (either BCK or WNB). Qualitatively similar findings apply for the global gas fraction, in agreement with ED17.

We conclude that the gas fraction within the bar is so low, that in TNG50 it is not responsible for whether a BP forms or not.

8 DISCUSSION

8.1 BP fraction at low and high stellar mass

We now interpret the behaviour of $f_{\text{BP}}(M_*)$ seen in Fig. 1. We assign an approximate stellar mass at which the plateau in $f_{\text{BP}}(M_*)$ begins, using the logistic regression fit for ‘All BPs’ in Table 3. We set this at the point where $f_{\text{BP}}(M_*)$ reaches 95 percent of the asymptotic fraction $K (= 0.59)$, which yields $\log(M_*/M_\odot) = 10.50$. We are especially interested in why there are so few BPs at low stellar mass, since they mirror the observations. We also interpret why the profile has a plateau, why this occurs at $\log(M_*/M_\odot) \gtrsim 10.5$, and why it

⁵Spearman $\rho = 0.52$ with $p\text{-value} = 1.4 \times 10^{-14}$.

⁶Some of these studies define f_g as a fraction of the disc mass, which is different from our definition. See Table 1.

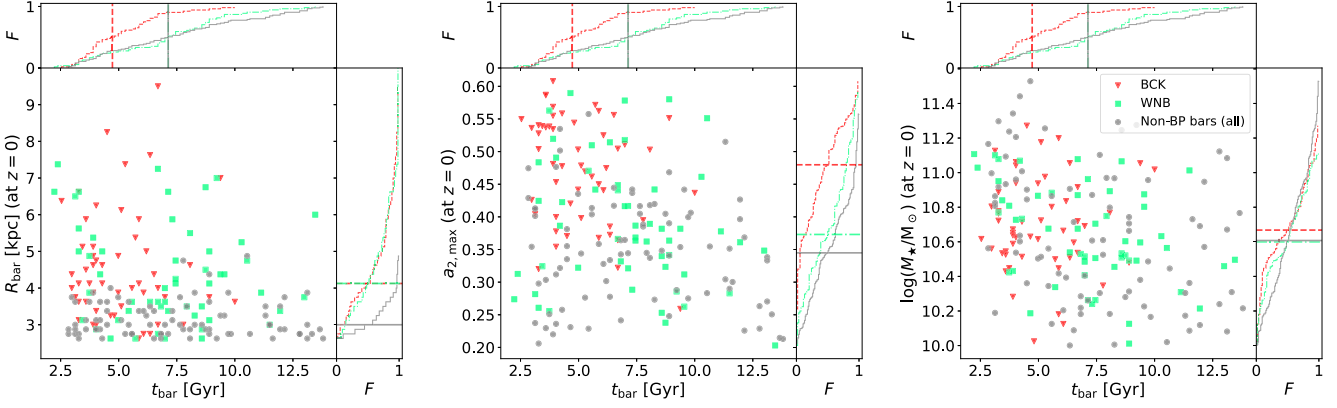


Figure 11. The distribution of barred galaxy samples in the $(t_{\text{bar}}, R_{\text{bar}})$, $(t_{\text{bar}}, a_{2,\text{max}})$, and $(t_{\text{bar}}, \log(M_*/M_\odot))$ planes, identifying BCK, WNB, and non-BP galaxies. The side panels represent cumulative distributions of the parameter on the respective axis, with their median shown in vertical (top) and horizontal (right) dashed lines. For clarity, the y-axis limit in the top panel is set to 10 kpc (there is one WNB galaxy at $R_{\text{bar}} = 13.6$ kpc, $t_{\text{bar}} = 9.55$ Gyr).

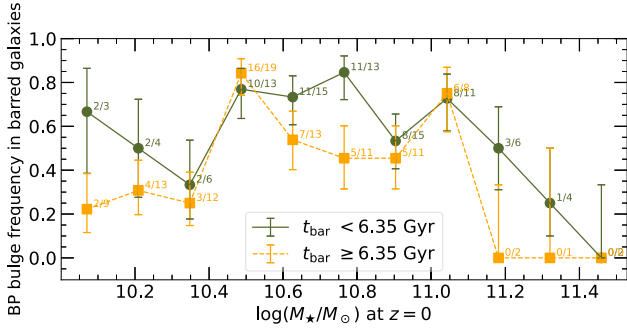


Figure 12. The fraction of barred galaxies hosting BPs at $z = 0$, split into young (orange dashed line, squares) and old (olive solid line, circles) populations, defined by median t_{bar} . The denominator in the fraction within each group is the number of barred galaxies within that group. Error bars are the 68 per cent (1σ) confidence limits from the Wilson (1927) binomial confidence interval.

asymptotes at ~ 0.6 in TNG50, whereas in observations the fraction saturates at 1 at high mass (ED17 and EDA23).

We define two mass bins: a low-mass bin before the plateau ($10.0 \leq \log(M_*/M_\odot) < 10.5$), and a high-mass bin ($10.5 \leq \log(M_*/M_\odot) \leq 11.2$), the latter covering the plateau region. This binning strategy is at the expense of having different numbers of galaxies in each bin (28 and 78 BP galaxies in the respective mass bins, and 34 and 42 galaxies for the non-BP galaxies). There are just 10 (of 191) galaxies with $\log(M_*/M_\odot) > 11.2$, and we do not show this bin on the plots for clarity since the dispersion in this bin would dominate the figures. Fig. 14 shows the evolution of various properties in each mass bin.

We examine first the low-mass regime where the BP fraction is low ($\lesssim 0.3$) but growing to ~ 0.6 at its high-mass end (Fig. 1). In Fig. 14, the low-mass bin (purple lines) has much lower f_{acc} than the higher mass bin. Despite this quiescent merger history, f_{BP} is low at this mass. Therefore, we can eliminate merger activity as the cause of suppression of the BP fraction at low mass.

We have shown that young bars are weaker than older bars, resulting in fewer BPs. Fig. 15 shows the median t_{bar} by stellar mass bin. It clearly shows the dominance of younger bars (higher t_{bar}) in the low-mass bin. At lower mass, BP bars are older (lower t_{bar})

than non-BP bars. Furthermore, amongst the BPs, we find that at low mass, there are more WNB than BCK galaxies (Fig. 1). Fig. 14 shows that $(\sigma_z/\sigma_R)_{\text{inbar}}$ is higher at low mass which suppresses buckling, since buckling requires low $(\sigma_z/\sigma_R)_{\text{inbar}}$. Also, Fig. 4 shows that at low mass, few bars are long, and those that are tend to have a high BP fraction. So in TNG50, at low mass, it is bar youth and their shorter, weaker bars, which cause a low BP fraction.

We now examine the high-mass regime. For all high-mass galaxies f_{acc} is higher from $z \sim 1$ than for low-mass galaxies (Fig. 14, upper panel). This is consistent with recent work by Guzmán-Ortega et al. (2023) who found that the merger fraction increases with stellar mass in both TNG50 and observations. Fig. 16 shows the $(\log(M_*/M_\odot), f_{\text{acc}})$, $(\log(M_*/M_\odot), a_{2,\text{max}})$ and $(a_{2,\text{max}}, f_{\text{acc}})$ planes for the BP and non-BP galaxies. It demonstrates that few BP galaxies with $f_{\text{acc}} \geq 0.2$ have $\log(M_*/M_\odot) \gtrsim 10.5$, where the plateau in $f_{\text{BP}}(M_*)$ begins. The figure also shows (middle panel) that, on average, bars are strongest at $\log(M_*/M_\odot) \sim 10.5$, but are weaker for higher mass galaxies. The left panel of the figure suggests this is due to a higher accreted fraction. The right panel reinforces this conclusion by showing the relation between f_{acc} and $a_{2,\text{max}}$, which reveals a declining bar strength with increasing f_{acc} at $z = 0$ (Spearman $\rho = -0.313$, $p = 1.1 \times 10^{-5}$). This is strong evidence that a greater accreted fraction is associated with weaker bars. Since f_{acc} increases with mass, why then does f_{BP} remain approximately flat at higher mass instead of declining?

We showed in Section 5.1 that in the barred sample, there is no monotonic relation between $\log(M_*/M_\odot)$ and R_{bar} , so the increase in f_{acc} is not compensated for by an increase in bar length. Fig. 14 shows a large difference in the high-mass bin between f_{acc} in the BPs (median 8 per cent) and the non-BPs (median 17 per cent), with the former having a noticeably narrower dispersion. This hints that a BP can develop up to a certain level of accretion (and consequent heating), but no further. Thus the formation of a BP may be neutral to the increase in merger activity as mass increases up to a point, holding f_{BP} flat. However, for the few galaxies with $\log(M_*/M_\odot) > 11.2$, perhaps the heating is so great that BP formation is mostly suppressed, which might explain why their f_{BP} is so low ($\lesssim 0.1$). The overall numbers at high mass are so small however, that we cannot draw any firm conclusions.

In summary, our analysis shows that, in TNG50, the reason for the non-BP bars' weakness is different in each mass regime – bar youth at low-mass, and merger activity at high mass. Downsizing (in the

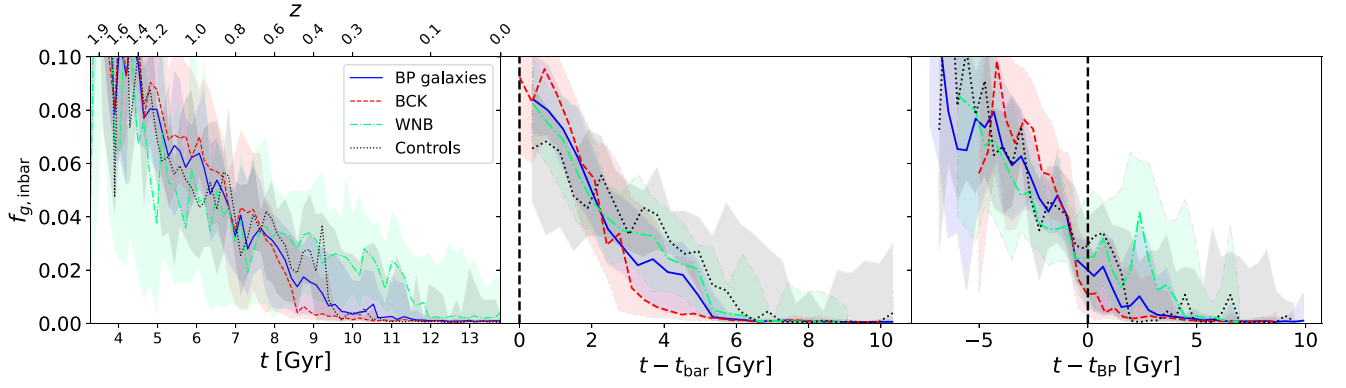


Figure 13. Evolution of the median $f_{g,\text{inbar}}$ for WNB, BCK, and BP galaxies, and for the controls. Left panel: the evolution of the median $f_{g,\text{inbar}}$ from $z = 2$. Middle panel: the evolution of the median $f_{g,\text{inbar}}$ as a function of $\Delta t = t - t_{\text{bar}}$ for each galaxy. $f_{g,\text{inbar}}$ is defined only after $t - t_{\text{bar}} = 0$ Gyr, represented by the vertical dashed black line. Right panel: the evolution of the median $f_{g,\text{inbar}}$ as a function of $\Delta t = t - t_{\text{BP}}$ for each galaxy (each control galaxy, with no BP by definition, is assigned the same t_{BP} as its mass-matched BP galaxy). The vertical dashed black line represents the time of BP formation, $t = t_{\text{BP}}$. In the two right panels we show only bins in Δt containing 10 or more galaxies. In the middle panel, we exclude 14 barred galaxies whose bars form before $z = 2$ since at these earlier times, the bar radius has high uncertainty. The shaded areas represent the 95 per cent confidence interval about the median from bootstrap resampling.

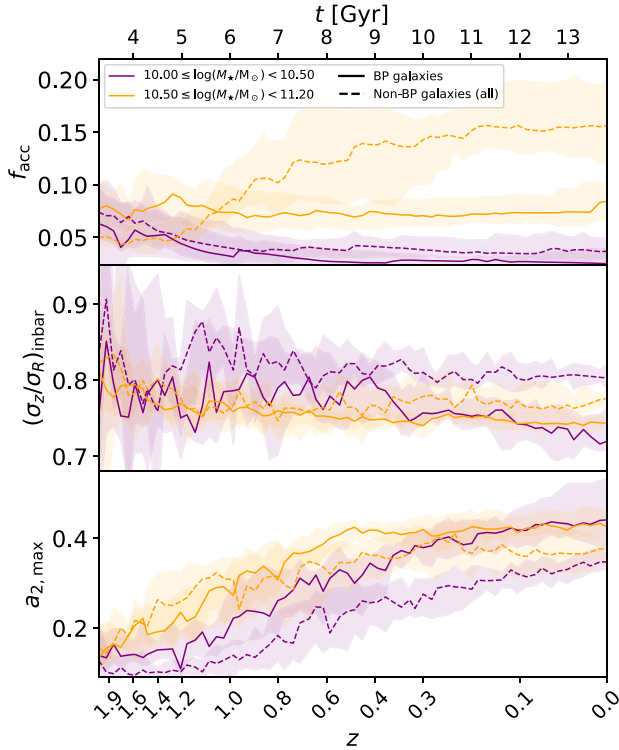


Figure 14. Evolution of the median f_{acc} (upper panel), $(\sigma_z/\sigma_R)_{\text{inbar}}$ (middle panel) and $a_{2,\text{max}}$ (lower panel) for BP (solid lines) and non-BP galaxies (dashed lines) by bins in M_* at $z = 0$, selected to match two key regions in the $f_{\text{BP}}(M_*)$ distribution (Fig. 1). The lowest and highest mass bins contain 28 and 78 galaxies in the BP sample, respectively. The corresponding numbers in the non-BP barred sample are 34 and 46. The shaded areas represent the 95 per cent confidence interval about the median from bootstrap resampling.

sense of bars being younger, hence weaker, in lower mass galaxies and older in higher mass galaxies) governs the *shape* of $f_{\text{BP}}(M_*)$ (the fact that it increases with mass to a plateau). Only above a certain mass are there enough sufficiently dynamically ‘mature’ bars to form BPs in significant numbers. The *value* of $f_{\text{BP}}(M_*)$ in a given mass bin

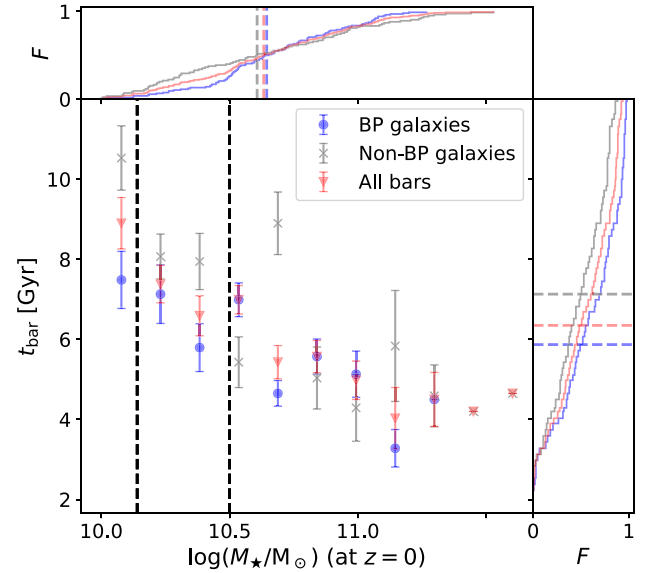


Figure 15. Median t_{bar} in bins of stellar mass for BP (blue circles), non-BP (grey crosses) and all barred galaxies (red triangles). The error bars represent the standard error on the median. The side panels represent cumulative distributions of the parameter on the respective axis, with their median shown in vertical (top) and horizontal (right) lines. Two vertical dashed black lines mark the turning point and the beginning of the plateau region in $f_{\text{BP}}(M_*)$ ($\log(M_*/M_\odot) = 10.13$ and 10.50 , respectively). At low mass, bars are significantly younger (higher t_{bar}) than at higher mass, contributing to suppression of the BP fraction.

is dependent both on the proportion of young and old bars, and on the accretion history of the galaxies in that mass bin. More generally, the heating of a barred galaxy is a key factor in determining its susceptibility to BP formation.

8.2 Comparison with observations

We caution that there are differences in the way barred galaxies and BPs have been selected here, and in observational studies. None the

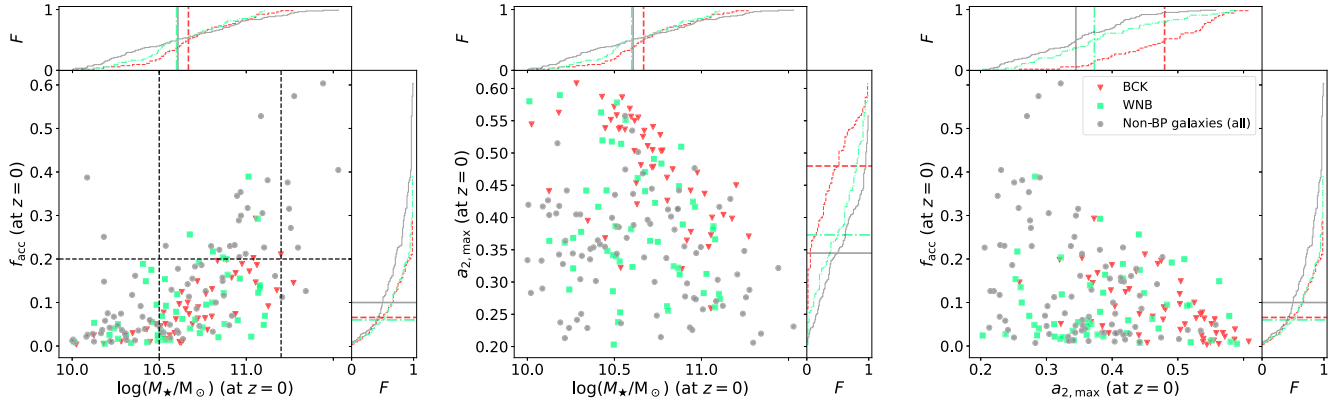


Figure 16. The distribution of barred galaxy samples in the $(\log(M_*/M_\odot), f_{\text{acc}})$ (left panel), $(\log(M_*/M_\odot), a_{2,\text{max}})$ (middle panel), and $(a_{2,\text{max}}, f_{\text{acc}})$ (right panel) planes at $z = 0$, identifying BCK, WNB, and non-BP galaxies. The side panels represent cumulative distributions of the parameter on the respective axis, with their median shown in vertical (top) and horizontal (right) lines. Dashed lines are inserted at $f_{\text{acc}} = 0.2$ and $\log(M_*/M_\odot) = 10.5$ and 11.2 in the left panel to guide the eye.

less, a comparison can provide further insights into how BPs develop in nature.

Owing to the caveats outlined in Section 2 we consider whether the BPs identified in TNG50 can be detected observationally. We sampled six approximately MW-stellar-mass galaxies from the BP sample, half of which were in the BCK subgroup, the other half in WNB. We generated mass maps with the galaxies at a few of the preferred orientations as determined by ED17. In only one case did we detect the ‘box + spurs’ morphology of a BP (Erwin & Debattista 2013). We believe our BP detection method therefore is able to find weak BPs which would be hard to detect observationally.

TNG50 does not match the stellar mass distribution of the BP fraction seen in observations (Fig. 1), although the overall fraction of 55 percent is close to, but somewhat lower than, observations. Yoshino & Yamauchi (2015) found a BP fraction of ~ 66 percent, and Kruk et al. (2019) found ~ 70 percent for example. It does however match the overall profile *shape* for $10.0 \lesssim \log(M_*/M_\odot) \lesssim 11.2$ (we have too few galaxies above this mass to make a credible assessment). Furthermore, this study finds a ‘turning point’ where f_{BP} reaches half its asymptotic high-mass value at $\log(M_T/M_\odot) \sim 10.1$, matching the sample of EDA23. ED17 found an upturn at $\log(M_T/M_\odot) \sim 10.4$ in their full sample (*i.e.* without the bar radius cut we adopt). In a sample of 1925 edge-on BP galaxies Marchuk et al. (2022) also found an upturn in f_{BP} at $\log(M_T/M_\odot) \sim 10.4$, albeit with a sample of unknown bar radius distribution. Thus the turning point we find is similar to that found in observations.

At low mass, where TNG50 closely matches the BP fraction in observations, bar youth (and hence weakness) may be a key driver of low BP fraction in nature. At higher mass it may be that the heating from mergers in the real Universe is simply not as efficient at inhibiting BP formation as we find in TNG50. At intermediate to high mass, galaxies in TNG50 may be too kinematically hot. Indeed, Wang, Pearson & Rodriguez-Gomez (2020) found that at $z = 0.15$, the major merger fraction in TNG100 matches observations reasonably well at $10.3 \lesssim \log(M_*/M_\odot) \lesssim 10.7$ (close to the turning point we find in f_{BP}), but is considerably (~ 50 percent) higher than observations above this mass (see their fig. 10). Observations show that bar length and strength are secondary variables in explaining whether a galaxy has a BP or not (EDA23 and ED17). Had the excessive heating been absent in TNG50, we speculate that f_{BP}

would in fact plateau at a higher level, and that $\log(M_*/M_\odot)$ would have the highest discriminatory power in determining whether a galaxy had a BP or not, rather than bar characteristics (Tables 4 and 5).

Despite the excessive heating overall, we have found that TNG50 BP galaxies have had a more quiescent merger history and had (relative to R_{eff}) thinner discs than non-BP galaxies at $z = 0$ (Sections 5.2 and 5.3).

8.3 Implications for the frequency of buckling

We have found no less than ~ 50 per cent of BP bulges at $z = 0$ in TNG50 which had at least one strong buckling episode in their history. There is reason to believe that, if anything, this fraction is an underestimate of the fraction in the real Universe.

Merritt & Sellwood (1994) showed that buckling can occur provided that a significant population of bar stars have vertical frequencies, ν , which are larger than the frequency with which they encounter the vertical forcing from the bar. For an $m = 2$ bending instability, this vertical forcing has frequency $2(\Omega - \Omega_p)$, where Ω is the angular frequency of the star and Ω_p is the pattern speed of the bar. Thus anything that causes ν to decrease inhibits buckling.

In TNG50, ν may be small for many stars. The softening length of TNG50 is 288 pc at $z = 0$. This is rather large in comparison to the thickness of the average disc galaxy (for example the Milky Way’s thin disc has scale height 300 pc, Bland-Hawthorn & Gerhard 2016). As a result, the vertical frequency of stars near the centres of galaxies are lower than they would be in a real galaxy with the same vertical density distribution (since the restoring force towards the plane is lower). Merritt & Sellwood (1994) show that, contrary to what might be naively expected, larger force softening *suppresses* buckling, rather than enhances it, because it reduces ν .

Furthermore, Ludlow et al. (2021) find that the relatively low dark matter (DM) particle resolution in cosmological simulations results in collisional heating both radially and vertically, albeit with a relatively small effect for TNG50 (the authors estimate a consequent increase in vertical scale height of 0.18 kpc). In their recent work, Wilkinson et al. (2023) showed that simulations are especially susceptible to spurious collisional heating if the number of DM particles $\lesssim 10^6$. In our work the median $\log(n_{\text{dark}}) \sim 5.7$

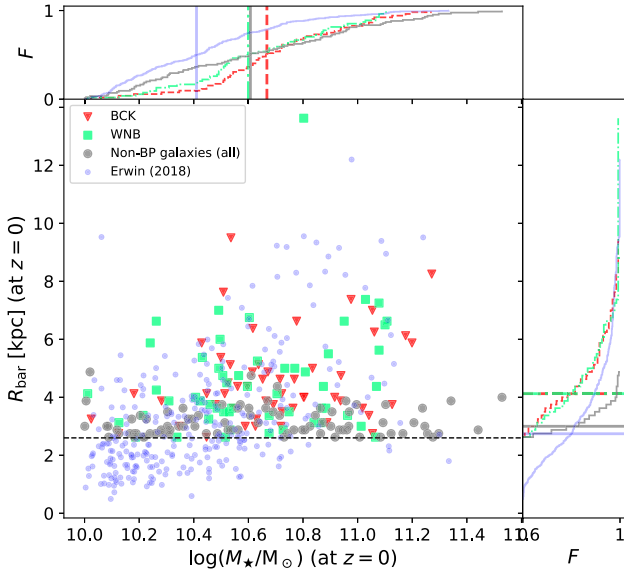


Figure 17. The distribution of barred galaxy samples in the $(\log(M_*/M_\odot), R_{\text{bar}})$ -plane at $z = 0$, identifying BCK, WNB, and non-BP galaxies. The side panels represent cumulative distributions of the parameter on the respective axis, with their median shown in vertical (top) and horizontal (right) panels. We overlay in light blue circles observational data from Erwin (2018) (see Section 8.3), with a cut on $\log(M_*/M_\odot) \geq 10.0$ to match the TNG50 sample (but without a cut on $R_{\text{bar}} \geq 2.6$ kpc). For these data, R_{bar} is the deprojected semi-major axis length of the bar. For the (Erwin 2018) data, to match the TNG50 sample, we show cumulative lines only for $R_{\text{bar}} \geq 2.6$ kpc. The horizontal black dashed line represents $R_{\text{bar}} = 2.6$ kpc.

(within $10R_{\text{eff}}$) for the barred sample at $z = 0$ in our sample and 90 per cent have $\log(n_{\text{dark}}) < 6.0$. So collisional heating may increase the thickness of the galaxies somewhat, especially for the lower-mass galaxies where the number of DM particles is small. This naturally leads to fewer BPs than if the galaxies were resolved with more DM particles. Sellwood, Nelson & Tremaine (1998) showed that the less well resolved a galaxy is, the easier it is for the disc to thicken. As TNG50 has a relatively large softening length we expect the discs may be somewhat thicker than those in nature. On the other hand, how severe this effect is might depend on the gas content of the disc, since kinematic heating of the gas disc may be radiated away, modulating its effect. Detailed investigation of this however is beyond the scope of this work.

Possible effects in cosmological simulations that may encourage buckling include strong bars possibly due to overly efficient removal of gas from the centres of the galaxies producing more radially anisotropic distributions at the centre. However, we find no evidence that TNG50 produces excessively strong bars. In Fig. 17, we show the $(\log(M_*/M_\odot), R_{\text{bar}})$ -plane and overlay in blue circles observational data from the Spitzer Survey of Stellar Structure in Galaxies (S⁴G, Sheth et al. 2010), taken from Erwin (2018). This is a distance- and magnitude-limited sample. Here, the bar radius is its deprojected semi-major axis length. We exclude galaxies with $\log(M_*/M_\odot) < 10.0$ to match the TNG50 sample. From this figure, it is clear that at $z = 0$, TNG50 does not produce excessively long (and by implication strong) bars compared to the observations. In TNG50 at $z = 0$, median $R_{\text{bar}} = 3.5^{+1.5}_{-0.8}$ kpc after the exclusion of bars smaller than 2.6 kpc, and $3.0^{+1.6}_{-0.8}$ kpc without excluding small bars (16th and 84th percentiles). The observational sample has bar lengths $4.0^{+2.1}_{-1.0}$ kpc after the exclusion of bars smaller than 2.6 kpc, and $2.7^{+2.3}_{-1.1}$ kpc for all bars.

Recent work by Frankel et al. (2022) concluded that TNG50 bars appear in general to be too short. This would contribute to the suppression of buckling in TNG50, yet about half (49 per cent) of its BPs (at least for $R_{\text{bar}} > 2.6$ kpc) are formed through this mechanism. Had buckling been more prevalent in TNG50, and all 45 non-BPs in the plateau region ($\log(M_*/M_\odot) \geq 10.5$ at $z = 0$) undergone strong buckling to be classified as BCK, the buckling fraction would be 97/151 or 64 per cent. Had they formed a BP through WNB mechanisms, the buckling fraction would be 52/151 or 34 per cent. We thus estimate that in nature, the fraction of BPs observed in the current epoch which had a strong buckling episode in their past is 49 ± 15 per cent. A higher percentage is more likely assuming some buckling suppression in TNG50.

Moreover, the fact that we find 7 galaxies, or $4^{+2}_{-1}\%$ of the barred sample have buckled recently (within 1.5 Gyr of $z = 0$) implies a significant probability of detecting recently buckled galaxies in the local Universe. Indeed, eight candidates have so far been identified (Erwin & Debattista 2016; Li, Ho & Barth 2017; Xiang et al. 2021).

9 SUMMARY

We have examined 191 barred galaxies with $\log(M_*/M_\odot) \geq 10.0$ and $R_{\text{bar}} \geq 2.6$ kpc from the TNG50 run of the IllustrisTNG simulation suite at $z = 0$ for the presence of box/peanut (BP) bulges. We have analysed the differences between those barred galaxies which have BPs at $z = 0$ and those which do not.

To find BPs, as well as inspection of density plots and unsharp images, we have used the fourth-order Gauss–Hermite moments of the vertical velocity distributions along the bar’s major axis. We use a metric developed from its profile to measure a BP’s ‘strength’ (akin to how well defined it is), and from this, the time of BP formation. We also track the time of bar formation, and the time of major buckling, if that occurs. Our main results are:

- (i) We identify 106 BPs among 191 barred galaxies at $z = 0$ (55 per cent). Of these, 52 (49 per cent) have buckled strongly at some stage in their evolution, and 54 (51 per cent) have not, presumably forming their BPs via resonant trapping, and/or weak buckling (Section 3).
- (ii) We find that bar characteristics (specifically length and strength) have the greatest discriminatory power in TNG50 in determining whether a barred galaxy has a BP or not, though this is in tension with observations (where stellar mass is the most important factor). The stronger and the longer the bars, the greater the fraction of them which host BPs (Section 4).
- (iii) We find the BP fraction amongst barred galaxies to be a strong function of stellar mass. TNG50 reproduces the overall shape and turning point ($\log(M_*/M_\odot) \sim 10.1$) of the distribution when compared with observations. It does not reproduce the observed fraction above $\log(M_*/M_\odot) \sim 10.5$, with TNG50 underproducing BPs at high mass (Section 3).
- (iv) Our analysis shows that those galaxies destined to have BPs at $z = 0$ have a more quiescent history than non-BP barred galaxies even when controlled for mass (consistent with the Auriga simulations). Their last major mergers occurred ~ 1.75 Gyr earlier than non-BP galaxies even when controlling for mass, and the latter also experienced many more minor mergers after this point. At $z = 0$, on average, the BP galaxies have median $f_{\text{acc}} \sim 6.3$ per cent versus 11.3 per cent in mass-matched controls (Section 5.3).
- (v) Galaxies destined to have BPs at $z = 0$ have thinner discs in relative terms, longer and stronger bars since $z \sim 1$, and their discs are

more radially anisotropic compared to non-BP galaxies, even when controlling for mass. Their bars are ~ 25 per cent stronger and ~ 40 per cent longer than bars in non-BP galaxies at $z = 0$. BPs require a host galaxy with low anisotropy (σ_z/σ_R) to form (Section 5.2).

(vi) In agreement with earlier observational studies, we find that the gas fraction has little discriminatory power as to whether a galaxy has a BP at $z = 0$. Within the bar, the gas fraction is so low that it has no influence on whether a BP forms or not (Section 7).

(vii) In TNG50, the low BP fraction at low mass is a consequence of bar youth, a manifestation of downsizing. Their youth means the bars are weaker, resulting in lower σ_R and higher σ_z/σ_R , suppressing BP formation (Section 8.1).

(viii) Higher mass non-BP galaxies have more past mergers than lower mass non-BP galaxies, suppressing BP formation. Heating from mergers, particularly at high mass, may be excessive in TNG50 compared to nature, resulting in the plateaued profile of the distribution of the BP fraction below that in observations (Section 8.1).

(ix) Our analysis suggests that buckling may be suppressed in TNG50, even though we find 49 per cent of $z = 0$ BPs having buckled in the past (excluding short bars). This implies that in nature, more than half (perhaps up to 65 per cent) of $z = 0$ BP bulges may have had a strong buckling episode in the past (Section 8.3).

ACKNOWLEDGEMENTS

We thank the anonymous referee for a thoughtful and constructive report, which has helped to improve the clarity of the paper. We also thank Annalisa Pillepich and Dylan Nelson for helpful discussions which improved the paper. SGK is supported by the Moses Holden Studentship. The IllustrisTNG simulations were undertaken with compute time awarded by the Gauss Centre for Supercomputing (GCS) under GCS Large-Scale Projects GCS-ILLU and GCS-DWAR on the GCS share of the supercomputer Hazel Hen at the High Performance Computing Center Stuttgart (HLRS), as well as on the machines of the Max Planck Computing and Data Facility (MPCDF) in Garching, Germany. Analysis of TNG50 galaxies was carried out on Stardynamics, a 64 core machine which was funded from Newton Advanced Fellowship # NA150272 awarded by the Royal Society and the Newton Fund. VC is supported by ANID-2022 FONDECYT postdoctoral grant no. 3220206. The analysis in this paper made use of the PYTHON packages JUPYTER, NUMPY, PYNBODY, and SCIPY (Pontzen et al. 2013; Kluyver et al. 2016; Harris et al. 2020; Virtanen et al. 2020). Figures in this work were produced using the PYTHON package MATPLOTLIB (Hunter 2007).

DATA AVAILABILITY

The data from the IllustrisTNG suite of simulations including TNG50 can be found at the website: <https://www.tng-project.org/data> (Nelson et al. 2019a).

REFERENCES

- Abbott C. G., Valluri M., Shen J., Debattista V. P., 2017, *MNRAS*, 470, 1526
- Aguirri J. A. L., Muñoz-Tuñón C., Varela A. M., Prieto M., 2000, *A&A*, 361, 841
- Akaike H., 1974, *IEEE Trans. Autom. Control*, 19, 716
- Algorry D. G. et al., 2017, *MNRAS*, 469, 1054
- Athanassoula E., 2002, *ApJ*, 569, L83
- Athanassoula E., 2003, *MNRAS*, 341, 1179
- Athanassoula E., Misiriotis A., 2002, *MNRAS*, 330, 35
- Berentzen I., Heller C. H., Shlosman I., Fricke K. J., 1998, *MNRAS*, 300, 49
- Berentzen I., Shlosman I., Martinez-Valpuesta I., Heller C. H., 2007, *ApJ*, 666, 189
- Bland-Hawthorn J., Gerhard O., 2016, *ARA&A*, 54, 529
- Blázquez-Calero G. et al., 2020, *MNRAS*, 491, 1800
- Buck T., Ness M. K., Macciò A. V., Obreja A., Dutton A. A., 2018, *ApJ*, 861, 88
- Bureau M., Athanassoula E., 2005, *ApJ*, 626, 159
- Butterworth S., 1930, *Exp. Wirel. Eng.*, 7, 536
- Ceverino D., Klypin A., 2007, *MNRAS*, 379, 1155
- Ciambur B. C., Fragkoudi F., Khoperskov S., Di Matteo P., Combes F., 2021, *MNRAS*, 503, 2203
- Combes F., Debbasch F., Friedli D., Pfenniger D., 1990, *A&A*, 233, 82
- Combes F., Sanders R. H., 1981, *A&A*, 96, 164
- Cuomo V. et al., 2022, *MNRAS*, 518, 2300
- Cuomo V., Aguerri J. A. L., Corsini E. M., Debattista V. P., 2020, *A&A*, 641, A111
- Cuomo V., Lee Y. H., Buttitta C., Aguerri J. A. L., Corsini E. M., Morelli L., 2021, *A&A*, 649, A30
- Davis M., Efstathiou G., Frenk C. S., White S. D. M., 1985, *ApJ*, 292, 371
- Debattista V. P., Carollo C. M., Mayer L., Moore B., 2005, *ApJ*, 628, 678
- Debattista V. P., Gonzalez O. A., Sanderson R. E., El-Badry K., Garrison-Kimmel S., Wetzel A., Faucher-Giguère C.-A., Hopkins P. F., 2019, *MNRAS*, 485, 5073
- Debattista V. P., Mayer L., Carollo C. M., Moore B., Wadsley J., Quinn T., 2006, *ApJ*, 645, 209
- Debattista V. P., Ness M., Gonzalez O. A., Freeman K., Zoccali M., Minniti D., 2017, *MNRAS*, 469, 1587
- Debattista V. P., Sellwood J. A., 1998, *ApJ*, 493, L5+
- Dolag K., Borgani S., Murante G., Springel V., 2009, *MNRAS*, 399, 497
- Du H., Mao S., Athanassoula E., Shen J., Pietrukowicz P., 2020, *MNRAS*, 498, 5629
- Du M., Debattista V. P., Shen J., Cappellari M., 2016, *ApJ*, 828, 14
- Du M., Ho L. C., Debattista V. P., Pillepich A., Nelson D., Hernquist L., Weinberger R., 2021, *ApJ*, 919, 135
- Dubinski J., Berentzen I., Shlosman I., 2009, *ApJ*, 697, 293
- Erwin P., 2005, *MNRAS*, 364, 283
- Erwin P., 2018, *MNRAS*, 474, 5372
- Erwin P., 2019, *MNRAS*, 489, 3553
- Erwin P., Debattista V. P., Anderson S. R., 2023, *MNRAS*, 524, 3166
- Erwin P., Debattista V. P., 2013, *MNRAS*, 431, 3060
- Erwin P., Debattista V. P., 2016, *ApJ*, 825, L30
- Erwin P., Debattista V. P., 2017, *MNRAS*, 468, 2058
- Eskridge P. B. et al., 2000, *AJ*, 119, 536
- Fragkoudi F. et al., 2020, *MNRAS*, 494, 5936
- Fragkoudi F., Di Matteo P., Haywood M., Gómez A., Combes F., Katz D., Semelin B., 2017, *A&A*, 606, A47
- Frankel N. et al., 2022, *ApJ*, 940, 61
- Gadotti D. A. et al., 2020, *A&A*, 643, A14
- Gargiulo I. D. et al., 2019, *MNRAS*, 489, 5742
- Gerhard O. E., 1993, *MNRAS*, 265, 213
- Ghosh S., Saha K., Di Matteo P., Combes F., 2021, *MNRAS*, 502, 3085
- Grand R. J. J. et al., 2017, *MNRAS*, 467, 179
- Grand R. J. J. et al., 2019, *MNRAS*, 490, 4786
- Guzmán-Ortega A., Rodríguez-Gómez V., Snyder G. F., Chamberlain K., Hernquist L., 2023, *MNRAS*, 519, 4920
- Harris C. R. et al., 2020, *Nature*, 585, 357
- Holley-Bockelmann K., Weinberg M., Katz N., 2005, *MNRAS*, 363, 991
- Hunter J. D., 2007, *Comput. Sci. Eng.*, 9, 90
- Khoperskov S., Bertin G., 2017, *A&A*, 597, A103
- Kluyver T. et al., 2016, in *Positioning and Power in Academic Publishing: Players, Agents and Agendas*. IOS Press, p. 87, <https://eprints.soton.ac.uk/403913/>
- Kormendy J., Kennicutt R. C., 2004, *ARA&A*, 42, 603
- Kruk S. J., Erwin P., Debattista V. P., Lintott C., 2019, *MNRAS*, 490, 4721
- Li X., Shlosman I., Pfenniger D., Heller C., 2023, *MNRAS*, 520, 1243
- Li Z.-Y., Ho L. C., Barth A. J., 2017, *ApJ*, 845, 87
- Lokas E. L., 2019, *A&A*, 629, A52
- Lokas E. L., 2020, *A&A*, 634, A122

- Ludlow A. D., Fall S. M., Schaye J., Obreschkow D., 2021, *MNRAS*, 508, 5114
- Lütticke R., Dettmar R.-J., Pohlen M., 2000, *A&AS*, 145, 405
- Marchuk A. A. et al., 2022, *MNRAS*, 512, 1371
- Marinacci F. et al., 2018, *MNRAS*, 480, 5113
- Marinova I., Jogee S., 2007, *ApJ*, 659, 1176
- Martinez-Valpuesta I., Shlosman I., 2004, *ApJ*, 613, L29
- Martinez-Valpuesta I., Shlosman I., Heller C., 2006, *ApJ*, 637, 214
- Matthews B. W., 1975, *Biochim. Biophys. Acta*, 405, 442
- McWilliam A., Zoccali M., 2010, *ApJ*, 724, 1491
- Méndez-Abreu J., Corsini E. M., Debattista V. P., De Rijcke S., Aguerri J. A. L., Pizzella A., 2008, *ApJ*, 679, L73
- Menéndez-Delmestre K., Sheth K., Schinnerer E., Jarrett T. H., Scoville N. Z., 2007, *ApJ*, 657, 790
- Merritt D., Sellwood J. A., 1994, *ApJ*, 425, 551
- Michel-Dansac L., Wozniak H., 2006, *A&A*, 452, 97
- Naiman J. P. et al., 2018, *MNRAS*, 477, 1206
- Nataf D. M., Udalski A., Gould A., Fouqué P., Stanek K. Z., 2010, *ApJ*, 721, L28
- Neistein E., van den Bosch F. C., Dekel A., 2006, *MNRAS*, 372, 933
- Nelson D. et al., 2018, *MNRAS*, 475, 624
- Nelson D. et al., 2019a, *Comput. Astrophys. Cosmol.*, 6, 2
- Nelson D. et al., 2019b, *MNRAS*, 490, 3234
- Pillepich A. et al., 2018, *MNRAS*, 473, 4077
- Pillepich A. et al., 2019, *MNRAS*, 490, 3196
- Pilyugin L. S., Thuan T. X., 2011, *ApJ*, 726, L23
- Pontzen A., Roškar R., Stinson G. S., Woods R., Reed D. M., Coles J., Quinn T. R., 2013, pynbody: Astrophysics Simulation Analysis for Python. Available at: <https://pynbody.github.io/pynbody/index.html>
- Purcell C. W., Bullock J. S., Kaplinghat M., 2009, *ApJ*, 703, 2275
- Qu Y., Di Matteo P., Lehnert M. D., van Driel W., 2011, *A&A*, 530, A10
- Quillen A. C., 2002, *AJ*, 124, 722
- Quinn P. J., Hernquist L., Fullagar D. P., 1993, *ApJ*, 403, 74
- Raha N., Sellwood J. A., James R. A., Kahn F. D., 1991, *Nature*, 352, 411
- Reshetnikov V., Combes F., 1996, *A&AS*, 116, 417
- Reshetnikov V., Combes F., 1997, *A&A*, 324, 80
- Rodionov S., Sotnikova N., 2013, *MNRAS*, 434, 2373
- Rodriguez-Gomez V. et al., 2015, *MNRAS*, 449, 49
- Rosas-Guevara Y. et al., 2020, *MNRAS*, 491, 2547
- Rosas-Guevara Y. et al., 2022, *MNRAS*, 512, 5339
- Saha K., Gerhard O., 2013, *MNRAS*, 430, 2039
- Saha K., Graham A. W., Rodríguez-Herranz I., 2018, *ApJ*, 852, 133
- Sales L. V., Navarro J. F., Schaye J., Dalla Vecchia C., Springel V., Booth C. M., 2010, *MNRAS*, 409, 1541
- Sellwood J. A., 1996, *ApJ*, 473, 733
- Sellwood J. A., Gerhard O., 2020, *MNRAS*, 495, 3175
- Sellwood J. A., Nelson R. W., Tremaine S., 1998, *ApJ*, 506, 590
- Sheth K. et al., 2008, *ApJ*, 675, 1141
- Sheth K. et al., 2010, *PASP*, 122, 1397
- Smirnov A. A., Sotnikova N. Y., 2019, *MNRAS*, 485, 1900
- Sotnikova N. Y., Rodionov S. A., 2003, *Astron. Lett.*, 29, 321
- Springel V. et al., 2018, *MNRAS*, 475, 676
- Springel V., White S. D. M., Tormen G., Kauffmann G., 2001, *MNRAS*, 328, 726
- Sugiura N., 1978, *Commun. Stat. A-Theor.*, A7, 13
- Toomre A., 1966, in *Geophysical Fluid Dynamics, notes on the 1966 Summer Study Program at the Woods Hole Oceanographic Institution*, ref. no. 66–46, p. 111
- van der Marel R. P., Franx M., 1993, *ApJ*, 407, 525
- Virtanen P. et al., 2020, *Nat. Methods*, 17, 261
- Vogelsberger M. et al., 2014a, *MNRAS*, 444, 1518
- Vogelsberger M. et al., 2014b, *Nature*, 509, 177
- Vogelsberger M., Marinacci F., Torrey P., Puchwein E., 2020, *Nat. Rev. Phys.*, 2, 42
- Wang L., Pearson W. J., Rodríguez-Gomez V., 2020, *A&A*, 644, A87
- Weinberg M. D., 1985, *MNRAS*, 213, 451
- Weinberger R. et al., 2017, *MNRAS*, 465, 3291
- Wilkinson M. J., Ludlow A. D., Lagos C. d. P., Fall S. M., Schaye J., Obreschkow D., 2023, *MNRAS*, 519, 5942
- Wilson E. B., 1927, *J. Am. Stat. Assoc.*, 22, 209
- Wozniak H., Michel-Dansac L., 2009, *A&A*, 494, 11
- Xiang K. M. et al., 2021, *ApJ*, 909, 125
- Yoshino A., Yamauchi C., 2015, *MNRAS*, 446, 3749
- Yule G., 1912, *J. R. Stat. Soc. Ser. C*, 75, 579
- Zhao D., Du M., Ho L. C., Debattista V. P., Shi J., 2020, *ApJ*, 904, 170

APPENDIX A: SAMPLE SELECTION

We describe here how barred and BP galaxies were selected from TNG50.

A1 Barred galaxies

Disc galaxies were selected at $z = 0$ following the method used by Zhao et al. (2020) with TNG100: we select those galaxies with stellar masses $M_* \geq 10^{10} M_\odot$ within a spherical radius of 30 kpc. We align the galaxy onto the (x, y) -plane using the angular momentum vector as described in Section 2. Disc galaxies are those with stellar kinematics dominated by ordered rotation using the K_{rot} parameter (Sales et al. 2010):

$$K_{\text{rot}} = \frac{1}{M} \sum_k \frac{m_k v_{\phi,k}^2}{v_{x,k}^2 + v_{y,k}^2 + v_{z,k}^2}, \quad (\text{A1})$$

where the sum is over all stellar particles k within the 30 kpc sphere, and M is the total stellar mass within the sphere. K_{rot} measures the fraction of stellar kinetic energy committed to in-plane rotation. Disc galaxies are defined as those having $K_{\text{rot}} \geq 0.5$ (Zhao et al. 2020). These cuts result in a sample of 608 disc galaxies at $z = 0$. We refer to this as the ‘disc sample’. For this sample, the number of stellar particles within $10R_{\text{eff}}$ is $1.7\text{--}96 \times 10^5$ (median 4.0×10^5) and the number of gas particles ranges from just 221 to 2.0×10^6 (median 2.1×10^5) at $z = 0$. From this point on, metrics are computed within a spherical radius of $10R_{\text{eff}}$ unless otherwise noted.

Since a bar is a bisymmetric deviation from axisymmetry, we define the global bar strength, A_{bar} , as the amplitude of the $m = 2$ Fourier moment of the stellar particle surface density distribution, projected onto the (x, y) -plane. We calculate the global bar amplitude as:

$$A_{\text{bar}} = \left| \frac{\sum_k m_k e^{2i\phi_k}}{\sum_k m_k} \right|, \quad (\text{A2})$$

where ϕ_k and m_k are the azimuthal angle and mass of each star particle. We compute the radial profile of a bar’s amplitude as:

$$a_2(R) = \left| \frac{\sum_{k,R} m_k e^{2i\phi_k}}{\sum_{k,R} m_k} \right|, \quad (\text{A3})$$

where now the sum runs over all stellar particles within a given cylindrical annulus of radius R . We also calculate the phase of the $m = 2$ Fourier moment within each annulus. Within the region where the $m = 2$ phase is constant to within 10° , we define the maximum of $a_2(R)$ as $a_{2,\text{max}}$. We consider a galaxy to be barred if $a_{2,\text{max}} > 0.2$. This results in a sample of 266 barred galaxies (44 per cent of the disc sample).

Many methods have been devised for measuring bar lengths, each having advantages and disadvantages (e.g. Aguerri et al. 2000; Athanassoula & Misiriotis 2002; Erwin 2005; Michel-Dansac & Wozniak 2006; Cuomo et al. 2021). At each time step in the

simulation for each barred galaxy identified above, we compute the bar's radius, R_{bar} , as the average of the cylindrical radius at which the amplitude of the $m = 2$ Fourier moment reaches half its maximum value (so $a_{2,\text{max}}/2$) after its peak, and the cylindrical radius at which the phase of the $m = 2$ component deviates from a constant by more than 10° beyond the peak in $a_2(R)$ (the median of half the difference between the two measures is ~ 20 per cent of the bar radius).

We restrict our attention to those BPs whose extent is at least twice the softening length (288 pc at $z = 0$) to be secure in our recognition of BPs. In their study of 84 moderately inclined local barred galaxies ED17 found that the range of sizes of the BP as a fraction of the bar radius is 0.25 – 0.76 (see also Lütticke, Dettmar & Pohlen 2000). To account for BPs of similar relative sizes, we require a minimum bar radius of ~ 2 kpc, and so we exclude galaxies with $R_{\text{bar}} < 2$ kpc. We argue in Appendix A4.2 for a more stringent cut of $R_{\text{bar}} < 2.6$ kpc. This more stringent cut eliminates 75 of the 266 barred galaxies, resulting in a final sample of 191 barred galaxies out of 608 (~ 31 per cent) disc galaxies.

We refer to this as the ‘barred sample’. We emphasize that it includes only those galaxies with bars at $z = 0$, whose radius is ≥ 2.6 kpc, having $a_{2,\text{max}} > 0.2$, and not those which may have formed bars which dissolved (or shrank to a radius < 2.6 kpc or weakened to below $a_{2,\text{max}} = 0.2$) before $z = 0$.

We note that Rosas-Guevara et al. (2022) (RG22) also studied barred galaxies in TNG50 with $\log(M_*/M_\odot) \geq 10$, with the total stellar mass defined as that enclosed within $10R_{\text{eff}}$ as in this study. Using the circularity parameter $\varepsilon = J_z/J(E)$ (where J_z is the specific angular momentum of a stellar particle around the z -axis, and $J(E)$ is the maximum specific angular momentum possible at the specific binding energy of the particle), disc particles were defined as those with $\varepsilon \geq 0.7$, and disc galaxies were defined as those with disc/total mass fraction > 50 per cent. Using this method, and a different bar length cut-off criteria than used in this study (RG22 used a bar radius limit based on the softening length), they found 349 discs and 105 (30 per cent) bars, compared to this study's 608 discs and 191 (31 per cent) bars.

The existence of a longer and stronger bar can perturb stars efficiently to dynamically hotter orbits. This mechanism can gradually reduce the mass fraction of stars with high ε . It is thus not surprising that the criterion used in RG22 found a smaller number of disc galaxies and barred galaxies. In Du et al. (2020, 2021), a careful decomposition of galaxies with $K_{\text{rot}} > 0.5$ showed that the mass ratios of their kinematically defined disk structures are larger than 50 per cent of the total stellar mass. We have also visually confirmed that the galaxies we selected using K_{rot} have clear disk structures. Therefore, we retain the use of K_{rot} in disc galaxy selection.

Fig. A1 shows the stellar mass distributions at $z = 0$ for the disc (608 galaxies), all barred (266 galaxies), barred with $R_{\text{bar}} \geq 2.6$ kpc (191 galaxies) and unbarred galaxies. The stellar mass distribution of the barred sample is similar to the mass distribution of all (*i.e.* including those with $R_{\text{bar}} < 2.6$ kpc) barred galaxies.

A2 Time of bar formation

Following Algorry et al. (2017), we track the evolution of the $m = 2$ Fourier amplitude for the barred sample, and set the threshold of bar formation at $a_{2,\text{max}} = 0.2$. We consider the bar to have formed when we detect at least four consecutive snapshots with $a_{2,\text{max}} > 0.2$, taking the formation time as the first step where this occurs. We denote this time as t_{bar} . Once this is identified, we compare with the

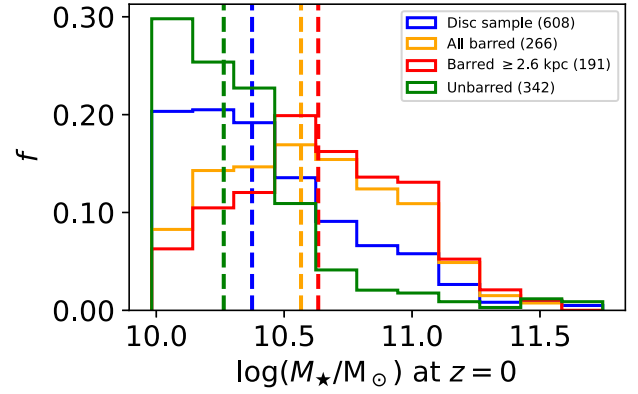


Figure A1. The distribution of stellar mass at $z = 0$ for all disc galaxies (disc sample – 608 galaxies, blue line), for all galaxies in the disc sample with bars ($a_{2,\text{max}} > 0.2$, 266 galaxies, orange line) and for the galaxies in the disc sample without bars (342 galaxies, green line) at $z = 0$. The red line shows the distribution for all bars within the disc sample with $R_{\text{bar}} \geq 2.6$ kpc (191 galaxies, see Appendix A1). The vertical dashed lines show the median stellar masses in each group.

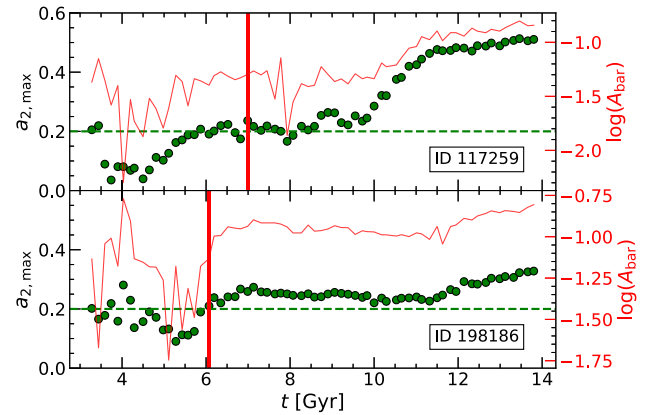


Figure A2. Bar formation time identification for two TNG50 barred galaxies. The horizontal green dashed line shows the $a_{2,\text{max}}$ threshold and the green points show $a_{2,\text{max}}$ values at each timestep. The solid red line shows $\log(A_{\text{bar}})$ at each step. The thick red vertical lines indicate the time of bar formation, defined in Appendix A2. The galaxies are labelled with their TNG50 Subhalo IDs.

evolution of A_{bar} . Since during bar formation the bar amplitude grows exponentially, after the instability has saturated we expect to see, at most, a slower secular growth. Therefore, we inspect the evolution of A_{bar} for each galaxy as a check on the reasonableness of the derived t_{bar} . Examples of this procedure are shown in Fig. A2, where A_{bar} stabilizes within two or three snapshots after t_{bar} . This figure also shows that bars can continue to grow after t_{bar} .

This method works well in 161 (84 per cent) of the barred galaxies, as confirmed by visual inspection of the density profiles. However, in 30 (16 per cent) barred galaxies, the evolution of A_{bar} and $a_{2,\text{max}}$ is too noisy to find t_{bar} within the algorithm's rules. In these cases, we inspect the (x, y) density distributions at each redshift and set t_{bar} manually. Note that 14 (7 per cent) of the bars have z_{bar} earlier than $z = 2$; in the middle panel of Fig. 13, the only place where this matters, we exclude these galaxies from the analysis.

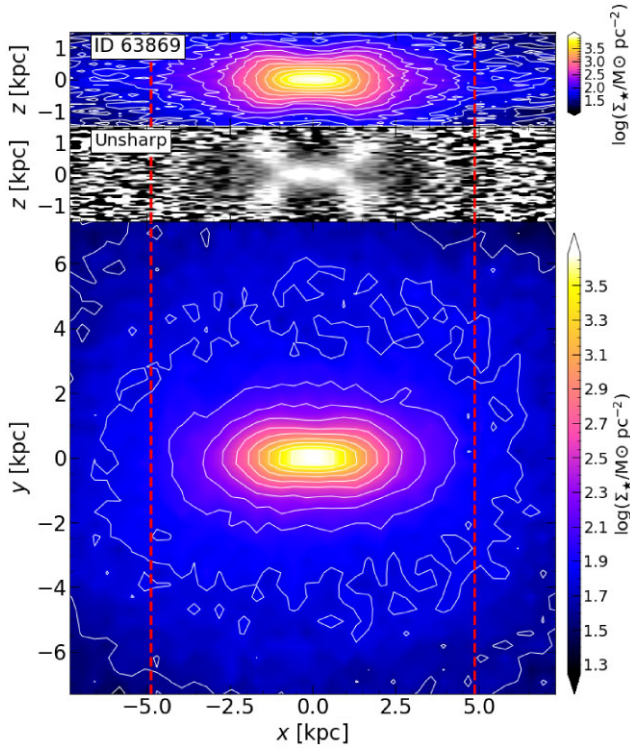


Figure A3. Example of (x, z) - and (x, y) -plane stellar density distributions (middle and bottom panels) and unsharp mask of the (x, z) distribution (top) for the barred galaxy 63869 at $z = 0$. The bar radius is indicated by the vertical red dashed lines. In the (x, z) projections, a cut of $|y| < 0.3R_{\text{bar}}$ is used. The ‘X’ shape of the BP bulge is apparent in the unsharp mask and pinching is visible in the (x, z) -plane density contours.

A3 Identification of BPs

We now describe our method for identifying BP bulges in barred galaxies at $z = 0$. We emphasize that we do not consider galaxies which may have had BPs at earlier epochs that do not survive to $z = 0$. Hence we do not study the evolution of the BP fraction as a function of redshift.

Starting with each barred galaxy at $z = 0$, we align the bar along the x -axis using the two-dimensional inertia tensor of the stellar density distribution in the (x, y) -plane. The tensor is computed within a cylindrical radius of R_{bar} (R_{bar} is found beforehand without the need to align the bar). We then identify BPs visually initially, and use a strength metric described in Appendix A4 for validation, and to provide a quantitative measure which we can track through each galaxy’s evolution. We examine density maps in the (x, z) (edge-on) plane, as well as unsharp masks of the edge-on density distribution. We use a cut of $|y| < 0.3R_{\text{bar}}$ to maximize the visibility of any BP component present whilst maintaining a reasonable particle count. The upper two panels of Fig. A3 show an example of the (x, z) -plane density plot and unsharp mask for one of the galaxies in the barred sample. In the bottom panel we also present the (x, y) surface density, where the bar extent is clearly visible. Note the pinched contours in the (x, z) -plane, which produces an ‘X’-shape in the unsharp mask, indicating the presence of a BP.

A4 Quantification of BP strength

The strength of a BP is a challenging concept to define, but is important for our analysis. Previous methods of determining the

BP strength have included using the median height (e.g. Fragkoudi et al. 2020), mass excesses when modelling the bulge as a spheroidal component (e.g. Abbott et al. 2017) and m -fold deviations from a pure ellipse in edge-on views (e.g. Ciambur et al. 2021).

In this work we measure the fourth order Gauss-Hermite moment of the vertical velocity distributions (Gerhard 1993; van der Marel & Franx 1993) along the bar’s major axis. The fourth order term in this series, h_4 , measures how peaked the distribution is compared to a Gaussian. If the distribution has $h_4 > 0$ at a particular point, then it is more sharply peaked than a Gaussian. If $h_4 < 0$ then the distribution is flatter than a Gaussian. Debattista et al. (2005) demonstrated that a BP bulge, when viewed face-on, produces two deep minima in the h_4 profile, on either side of the galactic centre along the bar major axis. This was confirmed observationally by Méndez-Abreu et al. (2008) in NGC 98. The minima appear because the vertical velocity distribution of stars is broadened by the presence of a BP. As did Debattista et al. (2005), in addition to the h_4 profile, we also examined the fourth order Gauss-Hermite moment of the height distribution along the bar major axis (d_4), but found this to be noisier and more challenging to constrain than h_4 . Thus for our BP strength metric we rely solely on h_4 .

We calculate the h_4 profile of v_z along the bar major axis (we continue to use a cut of $|y| \leq 0.3R_{\text{bar}}$ for each barred galaxy at every redshift, and identify the minima in h_4 on either side of $x = 0$, if present. A high signal-to-noise (S/N) ratio is required to compute accurate Gauss-Hermite moments. To achieve this, we bin along the bar major axis with an adaptive number of bins (found by experimentation) based on the particle count within the cut. We compute the S/N ratio as $\sqrt{N_p}$, where N_p is the particle count within each bin (Du et al. 2016). If we find minima in the resulting h_4 profile, we broaden the bins until we reach $S/N \geq 50$ at the location of the minima. To aid in detecting the peaks and valleys, we smooth the resulting h_4 profiles using a second-order Butterworth filter (Butterworth 1930) and interpolate using a cubic spline. We use the SIGNAL module of the PYTHON SCIPY library to search for peaks and valleys in the profiles, setting a limit λ on the number of extrema per kpc in the profile, rejecting any profile which has too many peaks or valleys per kpc as being too noisy. After some experimentation we set $\lambda = 1.75 \text{ kpc}^{-1}$. A profile without a valley on each side of $x = 0$ is deemed to be a non-BP profile. We avoid valley locations too close to the galactic centre (within 10 percent of the bar radius from the centre), and too close to the end of the bar (within 10 percent of the end). Selecting the deepest valley on each side of $x = 0$, we compute their mean, and denote this as $\overline{h_{4,\text{valley}}}$. We take the mean of the peak in h_4 between these two valleys (in many galaxies this frequently consists of just one broad peak), denoted as $\overline{h_{4,\text{peak}}}$, and use the difference as the peak–valley amplitude \mathcal{B} :

$$\mathcal{B} = \overline{h_{4,\text{peak}}} - \overline{h_{4,\text{valley}}}. \quad (\text{A4})$$

We use this dimensionless quantity as the BP strength metric, akin to its prominence. Its growth indicates large vertical excursions along the bar region, i.e. a BP bulge. We use the term ‘prominence’ as one can observe BP bulges which are large in physical size (radius) but appear as a weakly defined peanut, or smaller BPs in radius but with strongly defined ‘X’ shapes. So \mathcal{B} measures how well-defined the BP is. Hereafter, we use the term ‘BP strength’ throughout, on the understanding that this is a strength metric based on kinematics. Debattista et al. (2005) demonstrated a strong correlation between the fourth-order moment of the velocity and density, so we are satisfied with its suitability as a measure of BP strength. Uncertainties on \mathcal{B} are computed using the differences between the raw and smoothed h_4 profiles at the valleys and peak, added in quadrature.

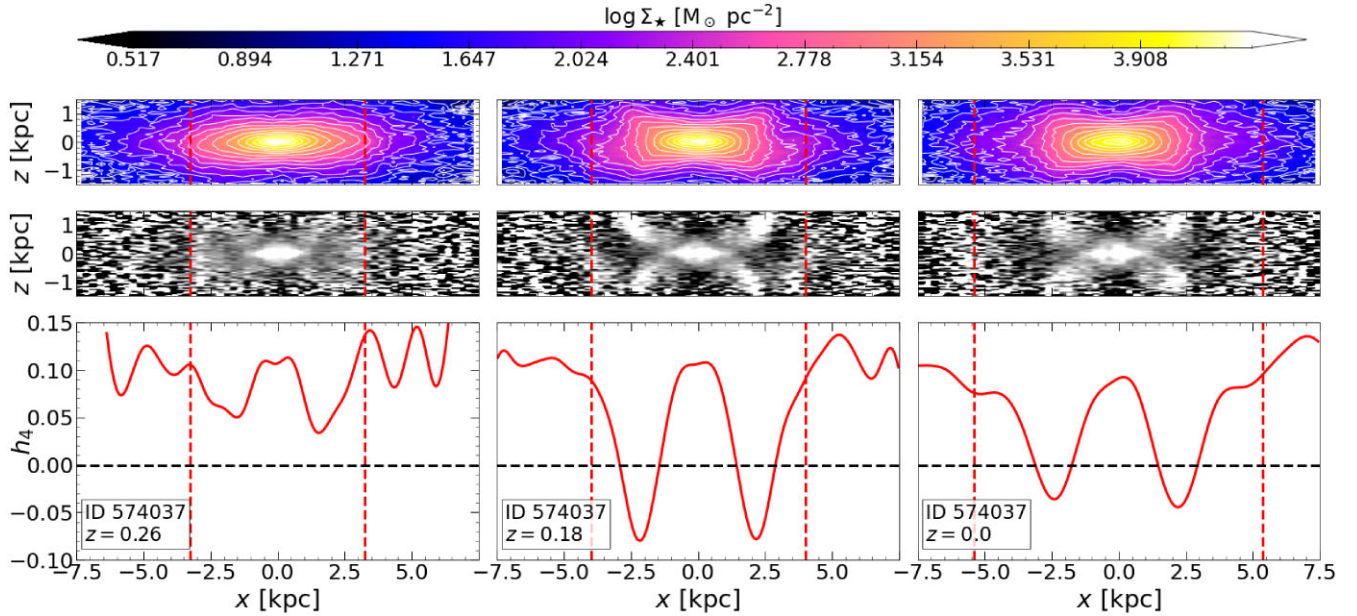


Figure A4. Example of a buckling galaxy, Subhalo ID **574037**, before, at and after its buckling redshift, $z = 0.18$. Top row: stellar surface density in the (x, z) -plane. Middle row: unsharp mask of the surface density in the (x, z) -plane. Bottom row: smoothed h_4 profiles along the bar major axis. Columns represent, from left to right, $z = 0.26, 0.18, 0$. The bar radius is indicated by the vertical red dashed lines. The black dashed line shows $h_4 = 0$ for reference. Each panel uses the cut $|y| < 0.3R_{\text{bar}}$.

Many bars without BPs have no detectable valleys in their h_4 profiles, and therefore have $\mathcal{B} = 0$.

A4.1 Buckling versus weak/non-buckling BPs

It is generally accepted that BPs can form via two principal mechanisms. The first is the most morphologically obvious – the buckling instability (Raha et al. 1991; Merritt & Sellwood 1994; Martinez-Valpuesta & Shlosman 2004; Erwin & Debattista 2016; Smirnov & Sotnikova 2019), a large deviation from vertical symmetry, followed by a rapid rise in vertical thickness in the inner regions of the bar. The second pathway is a BP which grows via the resonant trapping of stars, albeit more gradually (Combes & Sanders 1981; Combes et al. 1990; Quillen 2002; Sellwood & Gerhard 2020). This can be difficult to distinguish from weak buckling. (Recently, Li et al. (2023) demonstrated a link between overlapping planar and vertical 2:1 resonances and the buckling instability, providing a link between resonant excitation and buckling. This hints that the two pathways to a BP may not be as distinct as previously thought, although as we show, buckling is very evident in the evolution of \mathcal{B} .)

It is possible that some galaxies can form and grow their BP bulge through a mixture of buckling and resonant trapping which is difficult to disentangle. We distinguish those BP bulges which experienced a strong buckling episode in their history and those which did not. In isolated simulations, buckling happens rather rapidly, in $\sim 0.5 - 1$ Gyr (e.g. Martinez-Valpuesta & Shlosman 2004; Martinez-Valpuesta, Shlosman & Heller 2006; Lokas 2019; Cuomo et al. 2022; Li et al. 2023). This seems consistent with observations (e.g. Erwin & Debattista 2016). The minimum, maximum, and median difference between snapshots in TNG50 from $z = 2$ to 0 are 87, 236, and 159 Myr, respectively, thus providing good temporal resolution for detecting strong buckling. We note that strong buckling is obvious in (x, z) density distributions and unsharp mask images. It is accompanied by a strong signature in the h_4 profile (two deep

valleys appear on either side of $x = 0$), and hence a rapid increase in the BP strength, \mathcal{B} .

For each galaxy with a BP at $z = 0$, we examine unsharp mask images and density plots, noting if vertical asymmetry in the (x, z) -plane surface density map appears suddenly at any time, alongside the development of an asymmetric ‘X’ shape in the unsharp masks. If it does, and this is accompanied by the prompt formation of two deep valleys in the h_4 profile, and a steep rise in the evolution of \mathcal{B} , then we deem the galaxy to have experienced strong buckling. We label the time at which this occurs as t_{buck} and denote these galaxies as the ‘BCK sample’. An example is shown in Fig. A4 where the vertical asymmetry of galaxy **574037**, at the time of buckling, stands out in the stellar density, and the ‘X’ shape is visible in the unsharp mask. Note the evolution of the h_4 profile (bottom row) where we see the clear formation of two deep valleys on either side of $x = 0$ at buckling. After buckling, there is a reduction in the depth of the valley in h_4 .

We investigated the use of other buckling indicators, such as A_{buck} (Debattista et al. 2006) and A_{1z} (Li et al. 2023), but found these to be very noisy in TNG50, unlike in isolated simulations. In TNG50, we found a sharp increase in \mathcal{B} (see the example in the top left panel of Fig. A10) to be a much more reliable indicator of buckling, because it is insensitive to small misalignments of galaxy inclination (up to $\sim 30^\circ$).

While strong buckling is obvious, we may miss examples of weak buckling, possibly classifying BPs which had weak (possibly recurrent) buckling episodes in their history as having formed via resonant capture. We define those BPs where we did not detect strong buckling as the weak/non-buckling (‘WNB’) sample.

Fig. A5 shows three h_4 profiles at $z = 0$ which we identify as BCK, WNB and non-BP barred galaxies. Note the deep minima with $h_4 < 0$ in the BP galaxy which has undergone buckling (consistent with the findings of Sellwood & Gerhard 2020). The minima in the WNB galaxy are not as deep, but still prominent. The non-BP h_4 profile

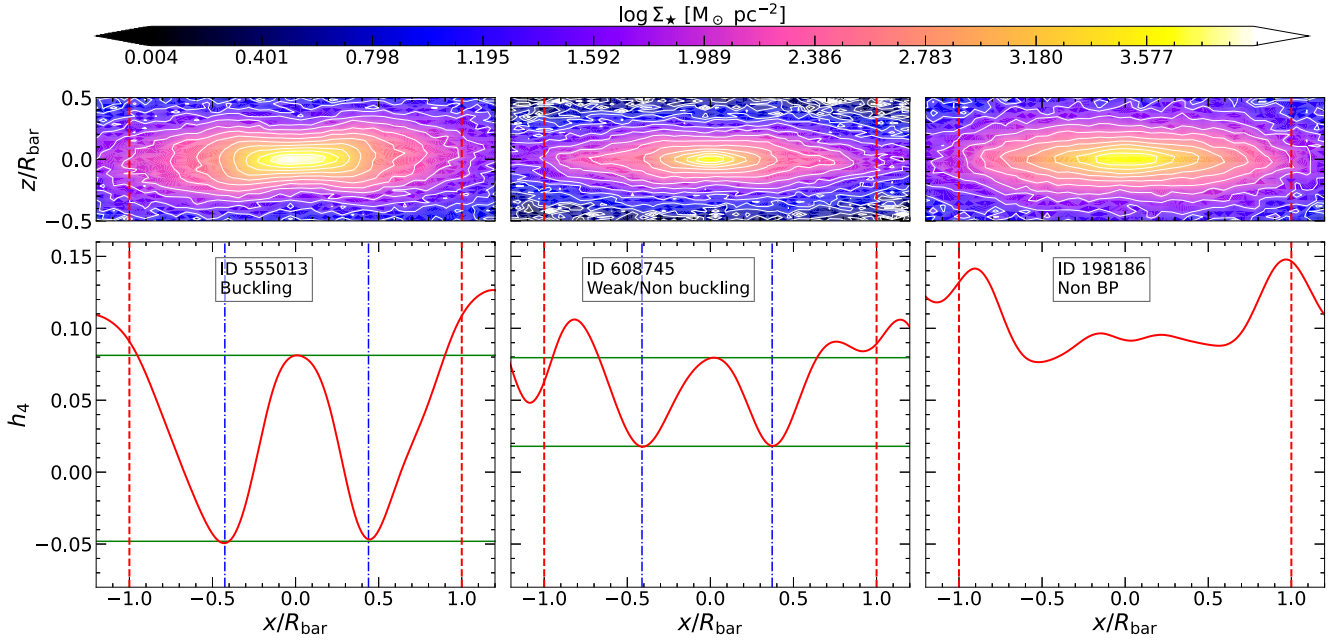


Figure A5. h_4 profiles along the bar major axis (bottom panels) for three galaxies at $z = 0$: a buckled BP galaxy (left column), a galaxy with a BP but which has no major buckling episode (middle column) and a barred galaxy without a BP (right column). The top panels show the stellar surface density in the (x, z) plane (vertical scale is shown as z/R_{bar}). All panels are shown for $|y| < 0.3R_{\text{bar}}$. The smoothed profiles are shown in solid red lines. The bar radius is indicated by the vertical red dashed lines. The two deep minima detected by the BP algorithm (blue vertical dot-dash lines) are present in the buckling galaxy, shallower ones in the weak/non-buckling galaxy, and the galaxy without a BP has a profile with shallow valleys. The green horizontal lines represent the mean valley and peak h_4 levels. The galaxies are labelled with their TNG50 Subhalo IDs.

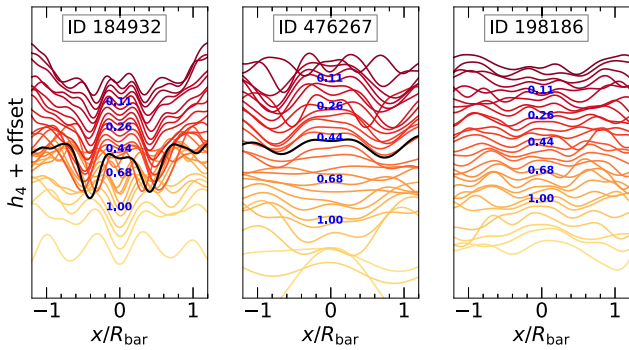


Figure A6. Examples of the evolution of the h_4 profiles along the bar major axis for three representative galaxies, a BCK (left panel), WNB (middle panel) and non-BP barred (right panel) galaxy. Time progresses upwards towards the darker colours, and we plot every other redshift from $z = 1.5$ for clarity. We apply a constant offset to separate the profiles vertically and every fifth time step, we label the redshift in blue. The profiles in solid black lines are those at the time of BP formation (Appendix A7). The galaxies are labelled with their TNG50 Subhalo IDs.

still has some peaks and valleys, but is considerably flatter in the central regions than the BP galaxies.

We illustrate the evolution of the h_4 profiles, from redshift $z = 1.5$ to $z = 0$, in Fig. A6 for representative BCK, WNB and non-BP barred galaxies. In the BCK and WNB galaxies, clear minima in h_4 are present after the BP forms, while the non-BP galaxy shows no such feature. The minima in buckling galaxies appear suddenly, and are deeper than in the WNB profiles.

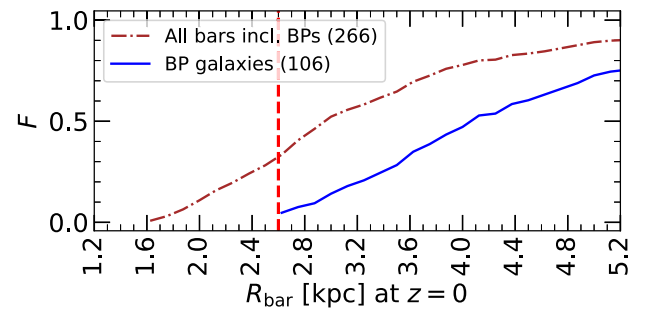


Figure A7. The cumulative distribution of R_{bar} for all barred galaxies (those with $a_{2,\text{max}} > 0.2$ but with no cut in R_{bar}) (brown dot-dashed line), and BP galaxies amongst them (blue solid line). To show details at small radius, the x -axis limit is set to ~ 5 kpc. The vertical dashed red line marks our bar cut, $R_{\text{bar}} = 2.6$ kpc.

A4.2 Refinement of the R_{bar} cut and final barred sample

Our initial bar radius cut was 2 kpc, based on arguments presented in Appendix A1. Fig. A7 shows the cumulative distribution of R_{bar} for BP and non-BP galaxies, which includes all bars with $a_{2,\text{max}} > 0.2$. We see that a cut of 2.6 kpc marks the radius where both cumulative fractions begin to rise linearly in a reasonably consistent way. Therefore, we select those bars with $a_{2,\text{max}} > 0.2$ and $R_{\text{bar}} \geq 2.6$ kpc as the barred sample. Compared to using a cut at $R_{\text{bar}} \geq 2$ kpc, this eliminates a further 58 barred and 5 BP galaxies.

After this cut, the visual inspection and BP strength determination results in a population of 106 BPs out of 191 galaxies in the barred sample (~ 55 per cent) at $z = 0$. We refer to those galaxies with a BP at $z = 0$ as the ‘BP sample’, while the remaining barred

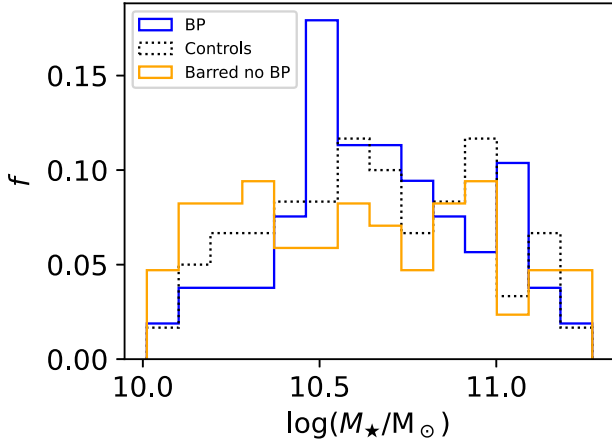


Figure A8. Distribution of $\log(M_*/M_\odot)$ for the BP (blue) and control (dotted black) samples at $z = 0$ and for comparison, all barred galaxies without BPs (orange). A good match between BP and control samples is achieved with a two-sample KS test having $p = 0.38$, signifying negligible difference in their distributions.

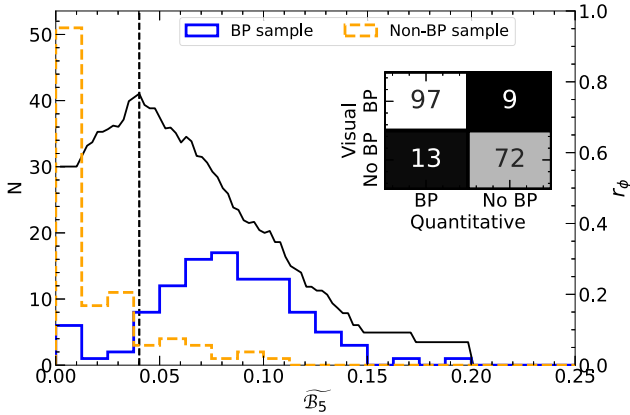


Figure A9. The distributions of the median of \mathcal{B} for the last five time steps, $\tilde{\mathcal{B}}_5$, for the BP (blue) and non-BP samples (orange) (left axis). The black line (right axis) shows r_ϕ , the ‘phi coefficient’ of Yule (1912); Matthews (1975), a correlation coefficient between the binary classifications methods, as a function of $\tilde{\mathcal{B}}_5$ which is used for the threshold value of BP classification. The confusion matrix in the top right corner is a comparison of the visual and quantitative classifications using the $\mathcal{B}_{\text{crit}}$ (maximum r_ϕ) value indicated by the vertical dashed line.

galaxies without BPs at $z = 0$ constitute the ‘non-BP sample’ (85 galaxies).

A5 Control sample

To help investigate the conditions which lead some barred galaxies to form BPs and others not, we produce a sample of non-BP barred galaxies which match the stellar mass distribution of our BP sample. For each BP galaxy, we select a barred but non-BP galaxy which is closest in terms of total stellar mass at $z = 0$. Although the matching is rather simple, it helps illuminate key differences in galaxy parameters, giving us insight into why those barred galaxies without BPs do not form them.

To construct the control sample, for every galaxy in the BP sample, we iterate through every galaxy in the non-BP barred sample to form

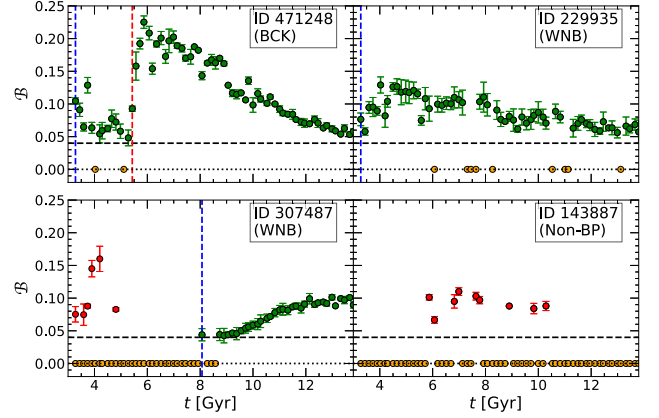


Figure A10. BP strength \mathcal{B} for four galaxies, one buckling, two WNB and one non-BP galaxy. The black dashed horizontal line shows $\mathcal{B}_{\text{crit}}$. Green points are those which meet our contiguity and threshold requirements for a BP, red those which do not (Appendix A7). The blue vertical dashed line marks t_{BP} , the time of BP formation (by definition, the non-BP galaxy has no BP at $z = 0$). The red dashed vertical line marks the time of buckling. The redshifts where the algorithm calculates no \mathcal{B} value are shown by the orange points along the x axis, and we mark $\mathcal{B} = 0$ with a dotted black horizontal line. The galaxies are labelled with their TNG50 Subhalo IDs.

combinations of each BP and a non-BP galaxy. For each combination, we calculate $\Delta M_*/M_*$, the fractional difference between the stellar masses at $z = 0$. These combinations are then sorted in ascending order by $\Delta M_*/M_*$ for matching. Since we have 84 non-BP galaxies (we exclude one which is in the process of buckling at $z = 0$), and 106 BP galaxies, we must pair some controls with more than one BP. To maximize the match in stellar mass, we allow each control to be used up to twice, *i.e.* pairing is done *with replacement*. 60 of 84 (71 per cent) unique control galaxies are paired amongst the BP galaxies. We refer to the population of control galaxies as ‘the control sample’.

Fig. A8 shows the distribution of M_* for BP and control galaxies. The BP galaxy and control stellar mass distributions have a two-sample KS test p -value of 0.38, signifying negligible differences between the two distributions. There are much larger differences between the BP sample and the population of non-BP galaxies ($p = 0.008$). Using this approach, 14 controls are paired once, 46 twice. The median fractional difference in M_* between BP galaxies and controls is 0.99 per cent. We find 96 per cent of BP galaxies have a fractional difference in stellar mass with their control of less than 5 per cent. Thus, when comparing BP and control galaxies, M_* is reasonably well controlled for.

A6 BP sample validation

We use the BP strength metric, \mathcal{B} , to perform a quantitative test of the BP sample obtained through visual inspection, since \mathcal{B} may be noisy, for example in cases of galaxies which experience interactions. We calculate the median of \mathcal{B} in the final five snapshots for each galaxy, $\tilde{\mathcal{B}}_5$, for the BP and non-BP samples and present their distributions in Fig. A9 (left axis). As expected, non-BP galaxies have near zero values of $\tilde{\mathcal{B}}_5$, with a tail to larger values (some galaxies have transient large values of \mathcal{B}). The BP sample clearly has overall larger values of $\tilde{\mathcal{B}}_5$ than the controls, with a large range. However, the distributions overlap. Using a single critical value of \mathcal{B} to classify barred galaxies as BP or non-BP would therefore introduce confusion in the classifications. We compare the visual and quantitative classifications based on applying a threshold $\mathcal{B}_{\text{crit}}$,

taking the visual classification to be the ‘truth’. We use the $\mathcal{B}_{\text{crit}}$ value to make a ‘predictive’ classification of each galaxy solely using each galaxy’s value of \mathcal{B}_5 (a BP being present if $\mathcal{B}_5 \geq \mathcal{B}_{\text{crit}}$).

We compute the mean square contingency coefficient, r_ϕ ,⁷ a correlation coefficient between binary classification methods (Yule 1912; Matthews 1975), as a function of $\mathcal{B}_{\text{crit}}$, then finding the value which results in the closest match to the visual classification. The r_ϕ value for each threshold value is also presented in Fig. A9 (right axis, black line). We find that a critical value of $\mathcal{B}_5 = 0.040$ results in an r_ϕ value of 0.735, and an overall accuracy (number of true positives and negatives as a fraction of all classifications) of 86.9 per cent at reproducing the visual classification. The confusion matrix using this critical value is presented in the top right of Fig. A9. This demonstrates that the \mathcal{B} metric captures the BP component of the bulge well, with some uncertainty in the individual values as well as uncertainty in our visual classifications. While comparing BP classifications between authors gives minimal disagreement, this test demonstrates the challenge of identifying BPs with an automated routine even in simulations.

A7 Measuring the time of BP formation

We use the BP strength \mathcal{B} to determine the time of BP formation. We calculate \mathcal{B} at each time step, and set a threshold of $\mathcal{B}_{\text{crit}} = 0.040$ found in Appendix A6, considering that a BP is present when $\mathcal{B} > \mathcal{B}_{\text{crit}}$. We find the earliest time step with no more than four subsequent consecutive time-steps with \mathcal{B} below the threshold (or no value for \mathcal{B}). We consider this to be the time when the BP formed, which we denote as t_{BP} . The constraint on the reasonably contiguous nature of \mathcal{B} avoids early transient signals (perhaps caused by interactions) and spurious signals caused by poor alignment. It sets t_{BP} at an epoch around which a BP is firmly established. That is, a few ‘missing’ time-steps with $\mathcal{B} < 0.040$ would not cause us to discount a time step being t_{BP} , unless this condition were protracted.

Fig. A10 shows examples of the evolution of \mathcal{B} for an example buckling (BCK) galaxy, two WNB galaxies and a non-BP galaxy, with their identified t_{BP} . We mark in green those points sufficiently contiguous in \mathcal{B} (and larger than $\mathcal{B}_{\text{crit}}$) for us to consider them a

suitable measure of BP strength. We see a sudden, rapid increase in \mathcal{B} at t_{buck} followed by a period of approximately linear decline in the buckled galaxy whose BP formed ~ 1 Gyr before buckling. The decline in \mathcal{B} is typical of buckling galaxies in TNG50, but varies across the sample. Sellwood & Gerhard (2020) noted an initially negative h_4 value immediately after buckling in their N -body models, which increased to around zero by the end of the evolution. The evolution of \mathcal{B} in the BCK galaxies is consistent with their result.

The evolution of \mathcal{B} in the WNB sample is more varied, as exemplified by the two WNB panels. Some exhibit an evolutionary pattern in \mathcal{B} similar to buckling galaxies (although in the unsharp masks and density we were unable to see evidence of any strong buckling in them), others show a steady increase in \mathcal{B} with time. Still others show a steady decrease in \mathcal{B} after an initial rise at t_{BP} , highlighting the difficulty in disentangling weak buckling from resonant capture-built BPs. We also verify the reasonableness of t_{BP} by visually inspecting the (x, z) density distributions and unsharp masks, ensuring a BP is discernible at this time.

⁷ $r_\phi = [(TP \times TN) - (FP \times FN)] / \sqrt{(TP + FP)(TP + FN)(TN + FP)(TN + FN)}$, where TP = number of true positives, TN = number of true negatives, FP = number of false positives, and FN = number of false negatives for each value of $\mathcal{B}_{\text{crit}}$ assessed.

For the non-BP galaxies, there is usually no pattern in the evolution of \mathcal{B} , and often no value could be calculated owing to a lack of a substantial h_4 peak–valley structure. Three controls do have some periods of contiguous evolution of \mathcal{B} before $z = 0$, but $\mathcal{B} < \mathcal{B}_{\text{crit}}$ at $z = 0$. They have indications of having had BPs in the past, but no longer at $z = 0$. Five controls have contiguous values of $\mathcal{B} > \mathcal{B}_{\text{crit}}$ up to $z = 0$ but no discernible BPs in the density plots and unsharp masks.

We check the consistency of t_{BP} and t_{bar} , checking those galaxies where t_{BP} was more than 1 Gyr before t_{bar} . This occurs in three galaxies and we reinspect these galaxies’ h_4 and density plots. We amend t_{BP} forward manually a few time steps in these cases.

This paper has been typeset from a \LaTeX file prepared by the author.